MINIREVIEW

Wafer scale growth of single crystal two-dimensional van der Waals materials

Chetna Gautam, [ID] [a] Baishali Thakurta, [ID] [b] Monalisa Pal, [ID] [b] Anup Kumar Ghosh [ID] *[a] and Anupam Giri [ID] *[c]

Two-dimensional (2D) van der Waals (vdW) materials, including graphene, hexagonal boron nitride (hBN), and metal dichalcogenides (MCs), form the basis of modern electronics and optoelectronics due to their unique electronic structure, chemical activity, and mechanical strength. Despite many proof-of-concept demonstrations so far, to fully realize their large-scale practical applications, especially in devices, wafer-scale single crystal atomically thin highly uniform films are indispensable. In this minireview, we present an overview on the strategies and highlight recent significant advances toward the synthesis of wafer-scale single crystal graphene, hBN, and MC 2D thin films. Currently, there are five distinct routes to synthesize wafer-scale single crystal 2D vdW thin films: (i) nucleation-controlled growth by suppressing the nucleation density, (ii) unidirectional alignment of multiple epitaxial nuclei and their seamless coalescence, (iii) self-collimation of randomly oriented grains on a molten metal, (iv) surface diffusion and epitaxial self-planarization and (v) seed-mediated 2D vertical epitaxy. Finally, the challenges that need to be addressed in future studies have also been described.

[a]Department of Physics, Institute of Science, Banaras Hindu University, Varanasi, UP – 221005, India. E-mail: akghosh@bhu.ac.in, anupamgiri@allduniv.ac.in
[b]Department of Chemistry, Institute of Science, Banaras Hindu University, Varanasi, UP – 221005, India
[c]Department of Chemistry, Faculty of Science, University of Allahabad, Prayagraj, UP-211002, India

1. Introduction

The growth of wafer-scale single-crystal (SC) two-dimensional (2D) van der Waals (vdW) layered thin films of a semimetal (graphene), semiconductors (MoS_2, $MoSe_2$, WS_2, WSe_2, *etc.*), and insulators (hBN) is critically important to enable the development of next generation 2D materials-based integrated electronics, optoelectronics, and spintronic devices for industrial applications.[1–6] The distinctive electro-mechano-optical pro-

Chetna Gautam received her B.Sc. degree in physics from Choudhary Charan Singh University (India) in 2016 and M.Sc. degree in applied physics from Babasaheb Bhimrao Ambedkar University (India) in 2018. She is pursuing her Ph.D. degree under the supervision of Prof. Anup Kumar Ghosh in physics at Banaras Hindu University (India). Her research interests include the synthesis of 2D transition metal dichalcogenides and their optoelectronic applications.

Chetna Gautam

Baishali Thakurta received her B.Sc. degree in chemistry from the University of Calcutta, India, in 2015 and M. Sc. degree in analytical chemistry from Jadavpur University, India, in 2019. She is pursuing her Ph.D. degree under the supervision of Dr Monalisa Pal at Banaras Hindu University (India). Her research interests include the facile synthesis of carbon-based nanomaterials and their applications.

Baishali Thakurta

perties, tunability of the bandgap and carrier density of 2D vdW layered materials and their heterostructures have also been considered to be ideal platforms for exploring novel physical optoelectronic properties,[7,8] charge density waves,[9,10] and superconductivity.[11–13] However, despite the impressive properties of 2D vdW layered materials, the lab-to-fab transition lags behind expectations, mainly due to the lack of (i) reproducible and scalable ways for the synthesis of large-area high-quality single crystal 2D vdW thin films and (ii) their easy integration into the established silicon-based fabrication lines.[14–17]

The device performance of polycrystalline 2D vdW thin films is not uniform throughout the film area due to nonuniformity in the grain sizes and the presence of grain boundaries. Therefore, to achieve satisfactory, reliable, and reproducible wafer-scale device performance on a par with the industry standard, high-throughput synthesis of wafer scale single crystal 2D vdW thin films is essential. Currently, there are three approaches to grow single crystal 2D vdW thin films: (i) growth from a single nucleus to a large single crystal film;[18] (ii) coalesce of unidirectionally aligned domains and their seamless stitching to a large single crystal;[19] and (iii) self-collimation and self-alignment of randomly oriented grains and their seamless stitching to a large single crystal.[20,21] While route (i) relies mainly on restricting the nucleation density at an extremely low level, the seamless stitching of unidirectionally aligned 2D domains *via* route (ii) requires a single crystal substrate with perfectly aligned step edges and epitaxial relationship with the lattices of the 2D vdW material. Route (iii) relies on the substrate assisted facile rotation of randomly oriented domains and eventual epitaxial self-collimation. Compared to the growth from a single nucleus (which takes many hours to produce one centimeter scale single crystals), epitaxial growth is more promising to produce large-area single crystal 2D vdW films at a much faster rate.

Usually, epitaxial growth is considered the method of choice for the synthesis of single-crystal 2D vdW thin films, but it requires single-crystal substrates with small lattice misfit ($7\% > \varepsilon_m > 0\%$) and a similar thermal expansion coefficient to the epilayer, to achieve conventional epitaxy. With a smaller lattice misfit, the epilayer film grows with one-to-one matching of lattice planes; however, when the difference in the lattice constants is larger, lattice strain in the epilayer film is created, which again increases with increasing film thickness. Very recently, several epitaxial growth methodologies have been reported for the production of wafer-scale single-crystal 2D vdW thin films of graphene, hBN and metal chalcogenides on high symmetry transition metal foil and film surfaces,[22–24] transition metal alloys,[25] Si (111),[21] Ge (111),[26] vicinal a/c-plane sapphire,[25,27–29] β-gallium(III) oxide (β-Ga_2O_3),[30] and gold (Au).[20,31,32] Benefiting from the aqueous solution's large-scale synthesis system, the direct thermal treatment of precursors to produce high-quality and wafer-scale 2D vdW thin films with controllable thickness on various substrates has been widely used and reported.[33–35] However, the 2D vdW thin films produced by these processes are polycrystalline in nature with grain sizes varying from nanometers to several hundreds of micrometers. There have been a few review articles covering the specific topics of 2D vdW nanomaterials including graphene,[36,37] hBN[3,38] and MCs.[4,39] Some reviews have focused exclusively on structural features,[4,40] electronic properties,[6,41] and applications of 2D vdW nanomaterials.[6,42,43]

In this minireview, we begin by providing the fundamentals of epitaxial growth of 2D vdW materials on high symmetry substrates. It is followed by an overview of recent successful representative achievements and the respective strategies adopted to produce wafer-scale single crystal graphene, hBN and metal chalcogenide (MC) thin films under epitaxial conditions. The mechanistic details of the strategies and the key experimental

Dr Monalisa Pal is currently an assistant professor at the Department of Chemistry, Institute of Science, Banaras Hindu University (BHU), Varanasi, India. She received her B.Sc. degree in chemistry from the University of Calcutta, India, in 2010 and M.Sc. degree in chemistry from IIT Delhi, India, in 2012. She completed her Ph.D. (chemistry, 2016) from S. N. Bose National Centre for Basic Sciences, India. Then she

Monalisa Pal

joined Prof. Unyong Jeong's group at POSTECH, South Korea, as a postdoctoral fellow and worked until 2020 before joining BHU. Her research interests include the synthesis of carbon-based nanomaterials and their applications in flexible electronics.

Prof. Anup Kumar Ghosh is currently a professor at Banaras Hindu University. He completed his Ph.D. degree in physics from Jadavpur University (India) in 1996. He completed his postdoctoral research as an ICTP fellow (1998) at the University of Rome "Tor Vargata" in Italy, a DFG fellow (2000) at the Darmstadt University of Technology in Germany and a JSPS postdoc fellow (2001) at the Tokyo Institute of Technology in Japan.

Anup Kumar Ghosh

His current research interests are the synthesis of 0D and 2D materials, multiferroics and diluted magnetic semiconductors.

parameters are described with some comments on their advantages and limitations. Finally, we summarize the future challenges and opportunities in the synthesis and industrial adaptability of wafer-scale single crystal 2D vdW thin films.

2. Driving forces for the on-substrate nucleation & growth of 2D vdW materials

During the formation of 2D vdW materials, the size of the nucleus is determined by the nucleation barrier, and the competition between the less stable surface atoms and the highly stable bulk atoms. Due to the higher edge formation energy, the nucleation barrier becomes higher, resulting in a lower nucleation rate. It enables the formation of a single nucleus of 2D vdW materials and determines the size of the nucleus on the substrate. During the initial growth, the clusters of 2D vdW materials adopt the energy-favored sites, whose registry is well preserved upon further growth owing to the strong interaction between the edge atoms and the underlying substrates.[44,45] In addition, edge structures play a critical role in controlling the growth kinetics and morphological evolution in 2D vdW materials.[46–51] There have been several review articles covering the role of geometries, energetics and stabilities of different edges of 2D nuclei and also on the role of different growth parameters (*e.g.* substrates, precursors, growth promoters, temperature, *etc.*) to govern the preferential growth and alignment of 2D vdW materials and thin films.[3,4,38,52–54] Since the edge formation energies of graphene are much higher over less active transition metal surfaces (*e.g.*, Au, Pd, Cu, *etc.*), it is easier to grow large grains of graphene over these surfaces *via* nucleation control.[48,55] Additionally, in the case of metal surfaces with step-edges, the lower nucleation barrier near the step-edges compared with the terraces, leads to a higher nucleation rate of graphene near the step-edges.[56] However, due to the multicomponent compositions of metal chalcogenides, and the passivation of metal atoms at the edges by chalcogen atoms, their edge formation energies are usually smaller than those of graphene and hBN, therefore, the control of the nucleation density of metal chalcogenides during CVD is far more challenging.[38] Crystal symmetry, lattice constant, miscut angle, microstructure, and surface energy are the major factors of a substrate which impact the shape, orientation, edge geometry, thickness, and surface coverage of the deposited 2D vdW thin films.[4,57] Fast diffusion of precursor atoms and the excellent catalytic ability of noble metal substrates such as Au and Pt, facilitates ultrafast growth of defect free uniform 2D graphene and h-BN layers.[22,58] Amorphous substrates (*e.g.* SiO_2/Si) and randomly oriented facets of polycrystalline substrates (*e.g.* noble and non-noble metal foils and films) generally lead to polycrystalline 2D vdW thin films, whereas, single crystal substrates such as Au (111), Pt (111), Cu (111), Ni (111), (0001) sapphire (α-Al_2O_3), Si (111), Ge (111), GaN and GaAs (111) may lead to aligned growth of 2D single-crystal domains or even highly oriented 2D vdW thin films. Based on recent theoretical calculations and experimental observations, the high symmetric edge of a 2D vdW material (*e.g.* ZZ directions of graphene, hBN and transition metal dichalcogenides) tends to align along a high symmetric direction of the substrate, such as the ⟨110⟩ directions of the Cu (111) and Au (111) surfaces, and the ⟨11$\bar{2}$0⟩ direction of hBN and Al_2O_3 (0001) surfaces. Therefore, to achieve the orientational uniformity of 2D vdW materials islands on a substrate, the 2D vdW material–substrate system should have the highest possible symmetry, which can be realized only if the symmetry group of the substrate is a subgroup of that of the 2D vdW material.[19,22,32,59] During graphene synthesis on Cu (111), carbon atoms are supplied through both surface diffusion and/or bulk segregation, and the continuous growth is enabled by the dissolution–diffusion–precipitation of carbon atoms on Cu (111). Therefore, both the surface carbon and dissolved bulk carbon atoms in Cu (111) play a critical role in the growth of graphene.[27] In contrast, the growth of hBN and metal chalcogenides on single crystal metal substrates follow surface chemical reaction mediated nucleation and growth of 2D seeds on the substrate surface, which depend on the interaction between 2D materials and substrates. So, the symmetry of the top layer atoms of the underlying metal substrate plays a critical role in determining the unidirectional epitaxial alignment of the grown overlayer hBN or metal chalcogenide grains.[52] Since both the Cu (111) surface and graphene have C_3 rotation symmetry and their lattice mismatch is as small as 4%, super-large single-crystal Cu (111) foil is ideal for epitaxial growth of large-size single-crystal graphene.[23] The formation of a large single-crystal graphene film has also been reported on the Cu/Ni (111) alloy foil surface *via* seamless merging of highly aligned graphene islands.[60] Although the face-centered cubic Cu (111) surface itself has a 3-fold symmetric structure,

Dr Anupam Giri is currently an assistant professor of chemistry at the Faculty of Science, University of Allahabad, Prayagraj, India. He received his B.Sc. (2007) and M.Sc. (2009) degrees in chemistry from the University of Calcutta (India). He completed his Ph.D. degree (chemistry, 2014) from S. N. Bose National Centre for Basic Sciences, India. As a postdoctoral fellow, he joined Prof. Unyong Jeong's group in 2014

Anupam Giri

and worked until 2020 at the Department of Materials Science and Engineering, POSTECH, Korea, before being promoted to the post of a research associate professor in the same department, where he worked until 2021. His research interests focus on the synthesis and electronic applications of two-dimensional materials.

atoms in its top-layer have a higher 6-fold symmetry (C_{6v}), leading to two anti-parallel domain alignment (differs by 60° or 180° orientations) configurations with near equivalent energy minima.[59] As hBN and transition metal dichalcogenide (TMDs) lattices have the same in-plane C_{3v} lower-symmetry, the Cu (111) surface with C_{6v} high-symmetry of the top-layer atoms, is not an appropriate template for the growth of single-crystal thin film of these materials due to the nucleation of antiparallel domains.[61] However, the unidirectional alignment of hBN domains was achieved over a large area (100 cm^2) on the Cu (110) vicinal surface, where the presence of metal step edges along the ⟨211⟩ direction led to a low C_1 symmetry, and facilitated strong coupling between the Cu step edges with hBN zigzag edges.[19] The most prominent feature of the step-edge facets is the presence of low coordinated surface atoms having rich, dangling bonds, which can easily interact with the reactants and facilitate near step-edge nucleation and uni-directional alignment of crystal domains.[19] In the case of TMDs, while growing on an insulating surface such as vicinal a-plane sapphire (a-Al$_2$O$_3$), due to the self-passivation of edge metal atoms by chalcogens, their interactions with the inert step edges of insulating surface are fairly different.[29] The epi-taxial growth of monolayer TMDCs is highly dependent on the guiding effect of substrate steps as well as the lattice symmetry of the underlying substrate. The low symmetry of the sapphire step edges restricts the formation of antiparallel domains and allows only one type of domain alignment to survive over the wafer-scale. Eventually the seamless stitching of the unidirec-tionally aligned domains leads to the formation of wafer scale single-crystal 2D TMD films.[28,29] Preferential lateral surface diffusion of chalcogens (*e.g.* Te and Se) in single-crystal metal surfaces (*e.g.* (111) Si, Ge), driven by favorable migration energy barriers, followed by spontaneous epitaxial flattening of the viscoelastic domains, can also lead to the formation of epi-taxial single-crystal 2D metal chalcogenide thin films on the wafer scale.[21]

3. Synthesis strategies for wafer-scale single crystal 2D vdW thin films

To date, different synthesis strategies have been applied to achieve wafer-scale 2D single crystal thin film growth of metals, semiconductors, and insulators, which are crucial for manufacturing high-performance electronic and optical devices. In this section, we present a detailed overview of strat-egies toward the synthesis of wafer-scale 2D single crystal thin films while highlighting the recent progress on graphene, hex-agonal boron nitride (hBN), and metal dichalcogenides.

3.1. Wafer-scale single crystal graphene thin films

Chemical vapor deposition (CVD) of carbon-containing precur-sors on catalytic substrates (*e.g.* Cu and Ni), involving a self-limiting growth mechanism, is currently the most promising route for the scalable synthesis of large-area, high-quality graphene films, and has also led to industrial-scale

production.[62–64] In recent years, to improve the quality of CVD-grown graphene, various strategies have been explored includ-ing complex substrate pretreatments and step-patterning, con-trolling the shape of the nucleated crystals, their registry and relative alignment over a large area.[39,41–43] In this section, we review the recent representative experimental realizations of the wafer-scale growth of single crystal graphene thin films *via* a nucleation density controlled growth mechanism and an epitaxy driven unidirectional grain alignment induced growth mechanism.

3.1.1. Nucleation controlled growth.
During CVD growth of graphene, the size of graphene domains is typically in the order of 10 μm, which is mainly due to the formation of huge numbers of graphene nuclei (10^6 cm^{-2}) at the initial nuclea-tion stage.[66,67] Therefore, several studies have been devoted to decrease the nucleation density for obtaining large-domain single crystal graphene films.[63,65,68–75] There are two main approaches for suppressing graphene nucleation site density. The first approach involves controlling the active sites of nucleation (sites with higher surface roughness and defect density or covered by impurity and contamination) on the growth substrates by means of reducing the number of active sites and passivation of active sites. For instance, several substrate pretreatment methods such as annealing,[69,73,76–78] chemical etching,[79–82] rinsing,[83,84] electrochemical polishing,[69,72,85] chemical mechanical polishing, *etc.*,[86] have been utilized for flattening and cleaning the substrate surface to reduce the number of active sites. Passivation of active sites in the growth substrates by using atomic oxygen (O),[70,73,76,87,88] and small organic molecules such as mela-mine,[89] 2-amino-4-methoxy-6-methyl-1,3,5-triazine[90] has been observed to drastically decrease the graphene nucleation density, facilitating the formation of centimeter-scale single-crystal graphene domains, and accelerating graphene domain growth. The second approach involves controlling the supply of active carbon species by local feeding of carbon source, repeated growth–etch–regrowth process, and multistage carbon supply. For instance, by locally feeding the carbon pre-cursors to the desired position of a Cu–Ni alloy substrate, Wu *et al.* demonstrated the formation of a 1.5-inch-large graphene monolayer in 2.5 h (Fig. 1a–d).[65] Fig. 1a, schematically shows the formation of a Cu–Ni alloy. As shown in Fig. 1b, the alloy with 15% Ni shows an optimum growth rate with a linear increase in the grain size after the incubation period. The alloy with a lower Ni content (*e.g.* 10% Ni) shows a surface-mediated growth mechanism like that on pure Cu, and the alloy with higher Ni content (*e.g.* 50% Ni) behaves more like pure Ni, yielding non-homogeneous multilayer graphene. In compari-son with global feeding, localized feeding induces the for-mation of a single nucleus on the entire substrate and greatly expedites the growth rate to form a monolayer film at a fast speed (Fig. 1c and d). Ding *et al.* have also demonstrated the site-selective nucleation of single-crystal graphene on Cu foil by spatial control of the carbon source (CH$_4$) using a perfo-rated Ni foil overlayer.[75] The catalytically active perforated Ni foil acts as a CH$_4$ modulator, resulting in the formation of
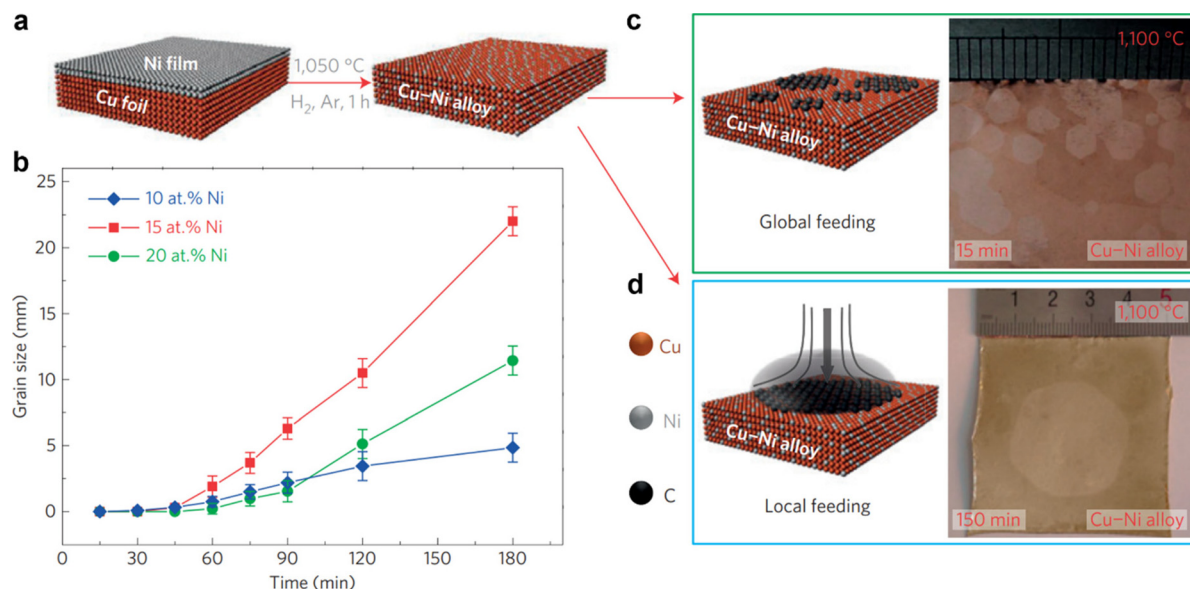
Fig. 1 (a) Schematic illustrations of the formation of the Cu–Ni alloy. (b) Comparison of graphene growth rates on different Cu–Ni alloy substrates at the growth temperature. (c) Schematic illustration of the global precursor feeding CVD process (left) and optical microscopy image of multiple nucleation and ultrafast growth of graphene (right) on the Cu85Ni15 alloy. (d) Schematic illustration of the local precursor feeding process (left) and optical microscopic image of a 2-inch size single crystal graphene film grown from a single nucleus (right). [Fig. 1 is reproduced with permission from Wu *et al.*[65] Copyright 2015, rights managed by the Nature Publishing Group].

millimeter-scale single-crystal grains at desired positions. Employing a "self-selection of the fastest-growing domain orientation" approach, Vlassiouk *et al.* demonstrated the formation of single-crystal like foot-long continuous graphene films at a rate of up to 2.5 cm h^{-1}.[63] Here the local hydrocarbon influx over the catalyst surface was controlled by varying the distance between the catalyst surface (Cu$_{90}$Ni$_{10}$ alloy substrate) and the nozzle hydrocarbon spreader in a moving substrate geometry, and also by increasing the flow rate of the high-velocity buffer gas (H$_2$–Ar).

Although the nucleation density can be reduced by the above mentioned growth strategies, inevitably, some new nuclei appear during growth, prohibiting the further growth of single-crystal graphene domains larger than the distance between the initial neighboring nuclei. Moreover, many structural defects are also commonly observed in the CVD-grown single-crystal graphene. Ma *et al.* demonstrated that the edges of graphene, which are the sites at which carbon accumulates in the 2D honeycomb lattice, significantly influence its growth. The growth and etching rate of the single-crystal graphene domain increase linearly with the slanted angle of its edges and are reversible in nature.[49] On the basis of this understanding, in a separate work Ma *et al.* developed a repeated growth–etching–regrowth (G–E–RG) process, to fabricate large-area defect-free single-crystal graphene.[91] Where a high CH$_4$ flow rate was applied for 10 min at the initial stage to enable rapid nucleation and growth of graphene domains. Then the flow of CH$_4$ was switched off and pure H$_2$ gas was introduced for 1 min to induce etching of newly formed nuclei, subsequently, H$_2$ gas supply was switched off and growth conditions were

reintroduced to grow the desired graphene domains further into a large-area single-crystal.

3.1.2. Unidirectional grain alignment and seamless coalescence driven growth. Although the nucleation-controlled growth by suppressing the nucleation density is an effective strategy to produce large-scale single crystal graphene, however, due to its lower growth rate it takes several hours to grow a fully covered wafer-scale graphene film. Nevertheless, because of the complicated experimental design and sensitivity of the process to control gas flow in the reactor, the process is not cost-effective. In contrast, unidirectional alignment of multiple epitaxial nuclei and their seamless coalescence into large-area single crystal graphene, have several advantages including shorter growth time and requirement of lesser stringent growth conditions. Lee *et al.* for the first time demonstrated the unidirectional epitaxial alignment of multiple graphene seeds on the H-terminated Ge (110) surface and the seamless merging of the aligned seed into uniform wafer-scale single-crystal graphene.[26] Where the asymmetric two-fold geometry of the Ge (110) surface and the anisotropic nature of the Ge–C covalent bonds dictate the perfect alignment of the edges of graphene seeds and their seamless merging.[92]

The Cu (111) surface plane is a more efficient and cheaper alternative to Ge (110) for its low lattice mismatch (~4%) with the honeycomb lattice of graphene, enabling epitaxially aligned nucleation and growth of graphene domains. For instance, Xu *et al.* has demonstrated the formation of a 5 × 50 cm^2 graphene film with >99% highly oriented grains within 20 minutes on single-crystal Cu (111) foil, facilitated by epitaxial growth of highly aligned graphene islands and their seam-

Fig. 2 (a) Cu (111) foils with graphene coverages of ∼60% (top panel), ∼90% (middle panel) and 100% (bottom panel), where the "shining" parts are graphene/Cu (left side). Three iPhone 6 devices are placed nearby as a reference. (b–d) Optical images of three regions of the graphene covered Cu (111) foil (marked as 1, 2, 3) in (a). (e) Schematics for the fabrication of wafer-scale single-crystal graphene on the Cu/Ni (111) alloy film at a low temperature. (f–h) Typical optical microscopy (OM) images of the evolution of graphene domains on the Cu/Ni (111) alloy film from individual grains to a continuous single crystal at 750 °C. [Fig. 2(a)–(d) are reproduced with permission from Xu *et al.* Copyright 2017, Elsevier Publishing Company. Fig. 2(e)–(h) are reproduced with permission from Zhang *et al.* Copyright 2019, Wiley-VCH, Weinheim].

less merging (Fig. 2a–d).[93] Fig. 2a shows Cu (111) foils with ∼60% (top), ∼90% (middle) and 100% (bottom) graphene coverage. Fig. 2b–d shows the Cu (111) foil areas with fully covered graphene, areas with aligned large graphene islands and areas with aligned small graphene islands, respectively.

The Pt (111) substrate is also of distinctive interest for the growth of high-quality graphene films, due to its similar carbon solubility similar to Cu (111) and relatively higher melting temperature (1768 °C) and lower thermal expansion coefficient than Cu. Therefore, compared to Cu (111), it can reduce the surface atom agglomeration and rough morphology under CVD growth conditions, thereby decreasing the nucleation density and point defects in graphene, and the density of wrinkles during the thermal quenching process.[94,95] Using Pt (111) as the growth substrate, Cheng *et al.* have grown a millimeter-sized defect-free single-crystal graphene film by the ambient-pressure CVD method and transfer these single-crystal graphene films to an arbitrary substrate, by using a nondestructive bubbling transfer method to enable the reuse of the Pt (111) substrate.[91,96] Kang *et al.* has recently reported the CVD growth of 6-inch single-crystal graphene on twinned Pt (111) films. The twinned structure of Pt (111) films does not change the preferential orientation of graphene nuclei, resulting in highly oriented graphene domains on the Pt (111) substrate.[97]

Huang *et al.* have recently reported fast growth (in 5 min or less) of large-area single crystal monolayer graphene over "homemade" single crystal Cu/Ni (111) alloy (1.3 at% to 8.6 at% Ni) foils.[60] Where the superstructure with Cu_6Ni_1 at the surface of these Cu/Ni alloy foils allows the epitaxial growth of highly aligned hexagonal graphene islands and their subsequent merger into highly oriented monolayer graphene over the entire substrate. However, this process requires a high growth temperature (1075 °C), which causes metal evaporation and sometimes wrinkles due to the large thermal expansion mismatch between the substrate and graphene during cooling.[98] Zhang *et al.* reported an alternative low temperature (750 °C) method using Cu/Ni (111)/sapphire wafers for epitaxial growth of 6 inch wafer-scale single-crystal graphene film after a 60 min growth (Fig. 2e–h).[99] Fig. 2e shows the schematic illustration of the two-step growth process and Fig. 2f–h shows the time dependent optical microscopy images of the evolution of graphene domains on the Cu/Ni (111) alloy film at 750 °C. The lower temperature requirement in this process could be due to either lower dehydrogenation energy of the carbon precursor, lower diffusion energy of carbon species on the Cu/Ni (111) alloy film surface, or lower energy barrier for attaching a carbon cluster to the as-formed graphene edge.

In a recent study, Li *et al.* have combined both the strategies nucleation control and unidirectional alignment of grains to
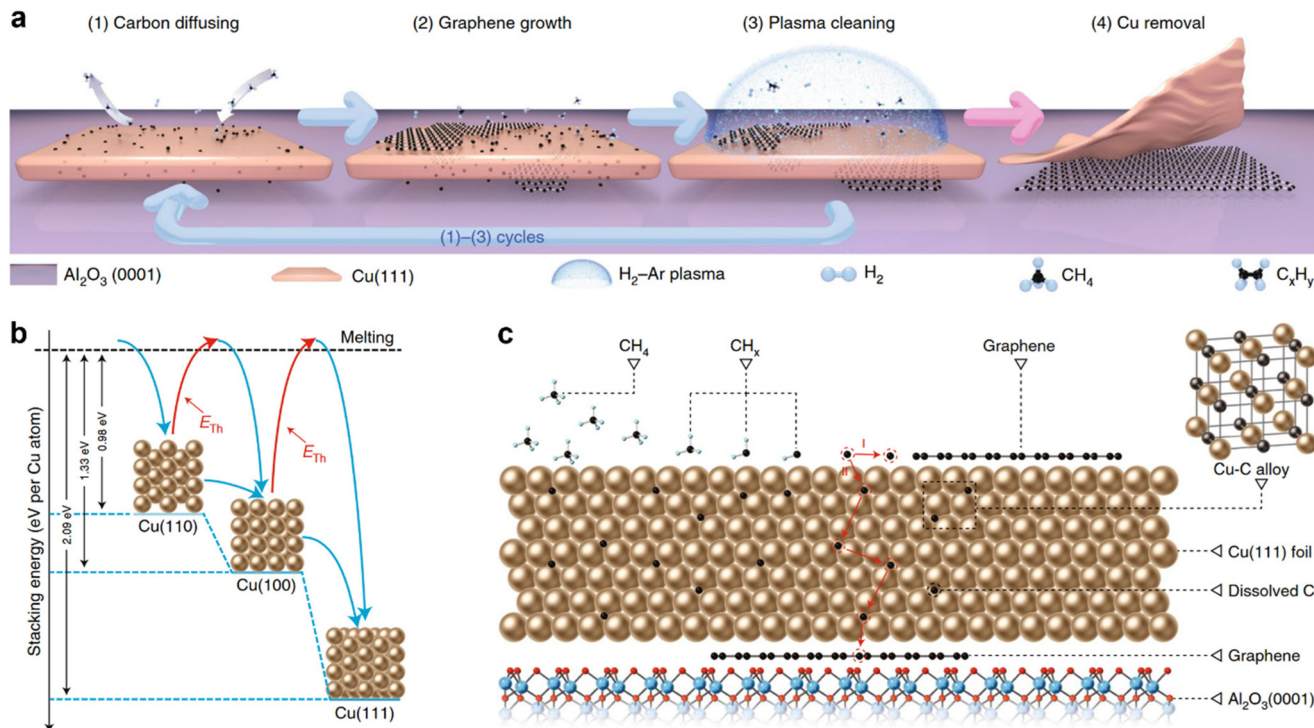
Fig. 3 (a) The synthesis scheme of wafer-scale single-crystal monolayer graphene thin film on electrically insulating Al_2O_3 (0001) wafers by a multi-cycle plasma etching-assisted-chemical vapor deposition (MPE–CVD) method. (b) Stacking energies of Cu (100), Cu (110) and Cu (111) on Al_2O_3 (0001). (c) Schematic showing the dissolution of carbon atoms in Cu (111) and the formation of a Cu–C alloy, which ensures continuous diffusion of carbon atoms to the Cu (111)–Al_2O_3 (0001) interface. [Fig. 3 is reproduced with permission from Li *et al.*[27] Copyright 2022, rights managed by the Nature Publishing Group].

produce wafer-scale single-crystal monolayer graphene on Cu (111)/Al_2O_3 (0001) wafers using a multi-cycle plasma etching-assisted-chemical vapor deposition (MPE-CVD) growth method (Fig. 3).[27] Fig. 3a schematically shows the four stages of the synthesis process, where the stage-1 (carbon diffusion), stage-2 (graphene growth) and stage-3 (plasma cleaning) reaction cycle was repeated many times until wafer-scale growth of single-crystal monolayer graphene at the interface between Cu (111) and Al_2O_3 (0001). Finally at stage-4, the Cu (111) film was bulged and peeled off to get inch-scale single-crystal graphene film directly on the insulating Al_2O_3 (0001) substrate. Graphene nucleation density at the Cu (111)–Al_2O_3 (0001) interface was controlled by tuning the graphene coverage (by means of plasma cleaning) on the top surface of Cu (111) and hence the diffusivity of the dissolved carbon atoms in and through Cu (111), which acts as carbon sources for graphene growth at the interface. It was found that the hexagonal shape and sharp edges of aligned graphene islands were formed at the Cu (111)–Al_2O_3 (0001) interface, which promotes the seamless merging of the graphene islands and produces a single-crystal wafer-scale as-grown graphene film. The effectiveness of this synthesis process relies on the hexagonal symmetry and the best lattice consistency with a minimal lattice mismatch of 6.5% between Cu (111) and Al_2O_3(0001). Moreover, the stacking energies per Cu atom were 0.98, 1.33 and 2.09 eV for Cu (110), Cu (100) and Cu (111), respectively, indicating that

Cu (111) is energetically favorable (Fig. 3b). Fig. 3c schematically shows the dissolution of carbon atoms in Cu (111) and the formation of a Cu–C alloy, which ensures continuous diffusion of carbon atoms to the Cu (111)–Al_2O_3 (0001) interface. Subsequently, the predominant formation of the graphene layer at the Cu (111)–Al_2O_3 (0001) interface was determined by the highest carbon binding energies of graphene (0.304 eV per carbon atom) at the Cu (111)–Al_2O_3 (0001) interface compared to Cu (111, 0.204 per carbon atom) and Al_2O_3 (0001, 0.200 per carbon atom). In a theoretical paper, Chen *et al.* discuss the kinetics and energetics of carbon nucleation in the early stages of graphene epitaxial growth on various metal surfaces.[100] The major interaction responsible for the preferential nucleation of graphene on various metal surfaces is listed in Table 1.

3.2. Synthesis of a wafer-scale single crystal hBN film

The CVD process is widely used to grow mono- or few-layer hBN on catalytic substrates, including Cu,[107–109] Ni,[110,111] Pt,[112,113] and Ru.[114] However, the typical grain size of CVD-grown monolayer hBN films are very small (usually <50 μm^2), because of the high nucleation density at the early growth stages, and the three-fold symmetry of the hBN lattice, which leads to antiparallel domains and twin boundaries on most substrates.[61,115,116] The small grains lead to high density of grain boundaries and dangling bonds, which are known as

Table 1 Different metal−graphene interactions

Metal substrates	Major interactions responsible for preferential nucleation of graphene	Ref.
Cu (111) and Cu (110)	Strong interaction between the graphene zigzag edge and the Cu ⟨110⟩ step edge leads to the unidirectional alignment of graphene islands on Cu (111) or Cu (110) substrates	Ref. 101
Ni (111) and Ni (110)	Strong interaction of graphene with the low-index Ni (111) and Ni (110) faces offsets the bending film stresses generated at terrace boundaries or at surface defects	Ref. 102
Pt (111)	Weak coupling of graphene to the Pt (111) substrate, leads to the existence of different rotational alignments and interface structures	Ref. 103
Pd (111)	Formation of Moire' superstructure patterns by the superposition of honeycomb lattice of graphene and hexagonal lattice of Pd (111)	Ref. 104
Ge (110)	Interaction between anisotropically arranged single-crystal Ge surface and graphene edges is responsible for the orientation determination of graphene seeds during nucleation and early stage of graphene growth	Ref. 26
Ir (111)	Precise epitaxial relation of the $\langle 11\bar{2}0 \rangle_C$ direction of C rows in graphene to the Ir surface dense-packed $\langle 10\bar{1} \rangle_{Ir}$ direction is satisfied at high growth temperatures of 1320 K	Ref. 105
Rh (111)	Bonding to the substrate is delocalized over the molecular π backbone of honeycomb carbon units (7C6 clusters), which essentially bind to the substrate *via* the peripheral carbon atoms	Ref. 106

structural defects in hBN.[117,118] Although micrometer-sized hBN grains have been commonly employed for fundamental studies,[119] wafer-scale single-crystal hBN (SC-hBN) films are not yet easily available for practical applications. In this section, we review the recent strategies adopted for the synthesis of wafer-scale single-crystal mono- or few-layer h-BN films.

3.2.1. Bulk metal foil and high symmetry metal film mediated growth. Compared to the C_{6v} symmetry of graphene, the lower symmetry (C_{3v}) of hBN makes the unidirectional alignment of hBN islands on a transition metal substrate (Cu, Ni, Pt, *etc.*) more challenging. Therefore, although 50 cm-scale single-crystal graphene has already been achieved using bulk Cu (111) foil as an epitaxial growth substrate, it is not a suitable substrate for the growth of single-crystal hBN due to the nucleation of antiparallel hBN domains. Using a low symmetry (σ_v or C_1) Cu (110) vicinal surface and low-pressure CVD method, Wang *et al.* demonstrated the epitaxial growth of a 100 cm^2 single crystal hBN monolayer.[19] Starting with an industrial Cu foil, single-crystal Cu foils with a Cu (110) vicinal surface were prepared using a designed high-temperature (1060 °C) pre-treatment process followed by long-time standard annealing treatment. The C_1 symmetry in Cu (110) originated due to the presence of metal steps along the ⟨211⟩ direction, which breaks the equivalence of antiparallel hBN domains and facilitates the coupling of Cu ⟨211⟩ step edges with hBN zigzag edges, resulting unidirectional alignment and seamless stitching of millions of hBN nuclei over a 100 cm^2 area. In a recent work, Ma *et al.* have demonstrated the epitaxial growth of a wafer-scale single-crystal tri-layer hBN film on single-crystal Ni (111) by the CVD method in 60 min at 1220 °C (Fig. 4).[24] Fig. 4a shows the scanning electron microscopy (SEM) images of the time dependent evolution of unidirectionally aligned tri-layer hBN islands (at 30 min), and their merger along one edge (at 45 min), into a fully covered tri-layer hBN film (at 60 min). Fig. 4b shows the schematic illustration of the growth process of individual tri-layer hBN islands. Where the process started with the dissociation of a borazine precursor on the Ni surface at 1220 °C followed by the dissolution of B into Ni as a solid solution. This triggers

the epitaxially aligned nucleation and growth of hBN islands. Finally, by coalescence of the aligned tri-layer hBN islands, the wafer-scale single crystal tri-layer hBN film was formed. Interestingly, during the cooling process, the appearance of the $Ni_{23}B_6$ film at the Ni (111)/hBN interface was observed, where the trilayer hBN/$Ni_{23}B_6$ and $Ni_{23}B_6$/Ni (111) layers show epitaxial relationships. During the growth process from the nuclei near the step edge, single crystal hBN propagated rapidly on the plateau between neighboring step edges. However, because of the extra energy requirement of hBN islands to cross the step edges, the growth rate is slow along the direction perpendicular to the step edges, therefore the islands become distorted trapezoid or truncated triangle-like in shape (Fig. 4c).[19] Similar growth kinetics has also been observed for hBN growth on a vicinal Cu (110) surface,[19] where, due to the presence of parallel step edges (from the uniform surface tilt angle) on the single-crystal vicinal Cu (110) surface led to unidirectionally aligned hBN domains (Fig. 4d). This edge-coupling-guided growth mechanism was also verified theoretically. The calculated formation energy for hBN growing on Cu (110) with steps along Cu ⟨211⟩ has a single minimum-energy state *i.e.* the most energetically preferred orientation, when the angle (γ) between the Cu ⟨211⟩ direction and the zigzag direction of the hBN nucleus is 0°.[19]

Although bulk single crystal Cu foil might be suitable for roll-to-roll production of single crystal hBN films, it is not compatible with the current microelectronic device fabrication line on wafers. Chen *et al.* have recently demonstrated wafer-scale epitaxial growth of single-crystal hBN monolayers on Cu (111) thin film deposited over a two-inch *c*-plane sapphire wafer (Fig. 5).[22] Where the epitaxial growth was facilitated by the lateral docking of hBN to the spontaneously present top-layer Cu (111) step edges, ensuring the mono-orientation of hBN monolayers by breaking the energy degeneracy of rotational twins differing by 60° or 180°. The growth of single-crystal hBN monolayers was carried out by flowing ammonia borane precursors onto the one-inch single-crystal Cu (111) thin film/ sapphire in a hot-wall CVD furnace. Fig. 5a shows the optical microscopy (OM) image of monolayer hBN triangular flakes

Fig. 4 (a) Scanning electron microscopy images showing the time-dependent growth process of trilayer hBN on a Ni (111) foil surface at 1220 °C. The inset show two different high-magnification SEM images, each showing hBN islands. (b) Schematic illustration of the proposed growth pathway of the trilayer hBN film on Ni (111) and the subsequent appearance of $Ni_{23}B_6$ at the Ni (111)/hBN interface. (c) Schematic illustration of hBN nucleation and growth on the Ni (111) surface. (d) Schematic diagrams highlighting the unidirectional growth of hBN domains and the anisotropic growth speed on a Cu surface with steps edges. (e) First-principles calculations of the formation energies of various hBN edges attached to a Cu ⟨211⟩ step on the Cu (110) substrate at different angle (γ). [Fig. 4(a)–(c) are reproduced with permission from Ma et al.[24] Copyright 2022, rights managed by the Nature Publishing Group. Fig. 4(d) and (e) are reproduced with permission from Wang et al.[19] Copyright 2019, rights managed by the Nature Publishing Group].

grown on a Cu (111) thin film with 60° in-plane rotated twin grains marked by blue and red dotted triangles. Whereas Fig. 5b shows the OM image of unidirectionally aligned monolayer hBN triangular flakes grown on a Cu (111) thin film, therefore, eliminating the possibility that twin hBN grain formation on Cu (111) is the critical factor to ensure the growth of single crystal hBN on the Cu (111) surface. Density functional theory (DFT) calculations were employed to investigate the epitaxy of the hBN seed (B_6N_7) at nucleation, with and without considering Cu (111) step-edge docking (Fig. 5c and d). Fig. 5c shows the lowest-energy atomic arrangements of six B_6N_7-Cu (111) units, considering the edge docking to two opposite step-edge terminations (A and B) of top-layer Cu (111). Where the B_6N_7 seeds are restricted to 0° (or 60°) orientation when docking to A (or B) steps. Based on the calculated binding energies of the six B_6N_7-Cu (111) configurations, B_6N_7 seeds should kinetically nucleate while docking to stronger binding sites, B types (edge-to-step), with suitable orientation, to ensure mono-orientated growth (Fig. 5d).

3.2.2. Molten metal surface assisted growth. The use of liquid Cu was found to be very effective at controlling the nucleation process and eliminating grain boundaries during the synthesis of uniform single layer, self-aligned graphene using the CVD process.[120] The approach involves the formation of a liquid Cu phase on quartz and W substrates at the growth temperatures above the Cu melting point. Where, to minimize the total surface/edge energy, the hexagonal graphene flakes translate and rotate into an edge-to-edge alignment on the liquid Cu surface, and finally evolve into a large single crystal graphene film by coalescence. Employing the same principle, Lee et al. demonstrated the formation of a wafer-scale single-crystal hBN film over a liquid Au surface by the CVD method (Fig. 6).[20] In this process, maintaining a flat Au with high surface tension is the key to allow strong adhesion of a borazine precursor. Then due to the limited solubility of boron (B, 0.5 atomic %) and nitrogen (N, ~0 atomic %) atoms in liquid Au (at 1100 °C), only surface diffusion of B and N adatoms on the surface of liquid Au at
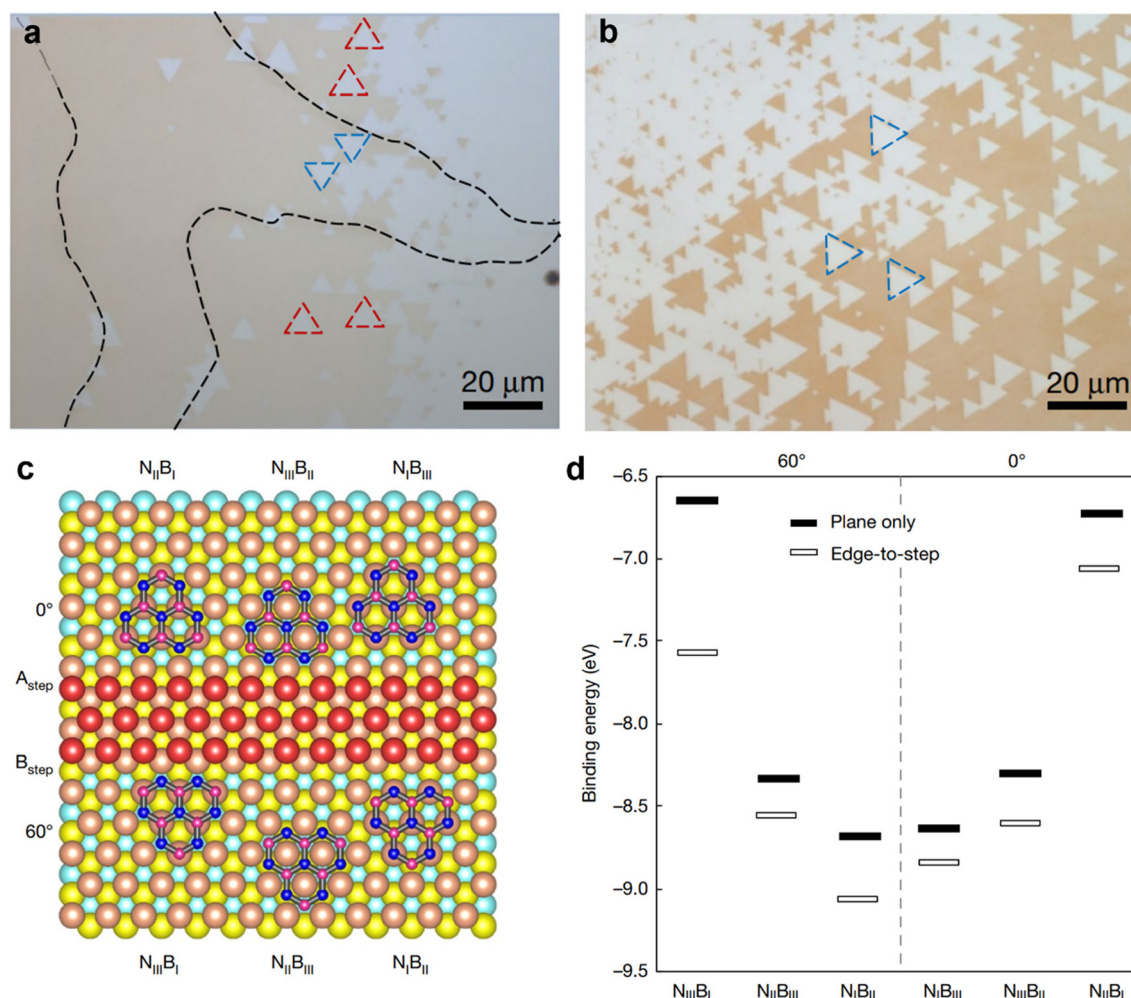
Fig. 5   (a) OM image of monolayer hBN triangular flakes grown on a Cu (111) thin film with 60° in-plane rotated twin grains marked by blue and red dotted triangles. (b) OM image of unidirectionally aligned monolayer hBN triangular flakes grown on a Cu (111) thin film. (c) The lowest-energy atomic arrangements of six B_6N_7-Cu (111) units, considering the edge docking to two opposite step-edge terminations (A and B) of top-layer Cu (111). (d) Calculated binding energies for the six B_6N_7-Cu (111) configurations, with and without including the edge-to-step epitaxy effect. [Fig. (a–d) are reproduced with permission from Chen et al.[22] Copyright 2020, rights managed by the Nature Publishing Group].

high temperature becomes prevalent, which promotes the formation of circular hBN grains. In the next step, due to the attractive electrostatic interactions between inter grain B and N atoms at the perimeter of each grain, the circular hBN grains rotated themselves to eventually self-collimate into the single-crystal hBN film on a wafer scale (Fig. 6a). Fig. 6b shows the time dependent SEM images of the growth process: (i) irregularly distributed circular hBN grains are formed at 30s, (ii) circular hBN grains with a regular size of ∼14.5 µm are formed at 10 min, (iii) density of hBN grains further increases without noticeable changes in size at 20 min, (iv) hBN grains are transformed further into a hexagonal close-packed structure by self-collimation at 30 min, (v) hBN coverage gradually increases and saturates to full coverage at 60 min growth time, and (vi) the hBN film is formed upon merging of hBN grains at 90 min. It is important to note that the hBN film obtained even after 90 min of growth time shows the presence of nano-

pores. Therefore, a two-step growth with an elevated growth time and additional precursor flow rate was applied to achieve the full coverage of a wafer-scale single crystal hBN film.

3.3.   Synthesis of wafer-scale single crystal metal chalcogenide (MC) films

Since the metal atoms are passivated by chalcogens at the edges of MCs, their edge formation energies are usually smaller than that of graphene and hBN. Therefore, the energy barrier for stable nuclei formation is smaller, making the process of controlling the nucleation density a challenging task. Experiments have also shown that it is very challenging to realize a very low nucleation density or only one nucleus over a large area.[121–123] In contrast, the multi-nucleation approach relies on a lattice-matched substrate, which enables the epitaxial MC domains to grow in the same orientation and then coalesce into a wafer-scale single crystal MC film.[93] In

Fig. 6 (a) Schematic illustration of the synthesis of the wafer-scale single crystal hexagonal boron nitride (hBN) film *via* self-collimation of randomly oriented grains on a liquid Au surface. (b) Scanning electron microscopy images of the hBN thin film growth process at different growth times. [Fig. 6 is reproduced with permission from Lee *et al.*[20] Copyright 2018, American Association for the Advancement of Science].

this section, we review the state-of-the-art strategies such as unidirectional seeding and nucleation at the vicinal step edges, epitaxial collimation, and seeded in-plane 2D-epitaxy, adopted to induce uniform domain orientation for the synthesis of wafer-scale single crystal MC films.

3.3.1. Unidirectional seeding and nucleation at the vicinal step edges/ledges. Various studies have been conducted on growing large-area MC films on epitaxial substrates, such as mica and sapphire.[124,125] However, because of the non-centrosymmetric C_{3v} lattice of MCs, the six-fold symmetry of such substrates has been found to be incompatible and generally leads to the equivalency of antiparallel islands (0 and 60° orientations) and inevitable twin boundaries.[126] Yang *et al.* first demonstrated the edge-mediated epitaxial growth of wafer-scale single crystal MoS_2 monolayers on vicinal Au (111)

thin films.[32] Where the unidirectional nucleation of MoS_2 domains is guided by the ⟨110⟩ step edges on Au (111), with the Mo_{zz} edge of MoS_2 directed along the ⟨110⟩ direction of the Au (111) surface. Following a similar strategy, Choi *et al.* have demonstrated the wafer-scale single crystal growth of MC monolayers (including WS_2, WSe_2, MoS_2, $MoSe_2/WSe_2$ heterostructure, and $W_{1-x}Mo_xS_2$ alloy) using an atomic sawtooth gold surface as a universal growth template.[31] Where the anisotropic adsorption energy of the MC cluster to the atomic-step edges, dictates the unidirectional epitaxial growth of triangular MC grains and eventual formation of single crystal MC films regardless of the Miller indices. Using a *c*-plane sapphire substrate with a predesigned miscut orientation perpendicular to the substrate surface (towards the *A* axis, C/A), Li *et al.* demonstrated the epitaxial growth of a 2 inch (~5 cm) thick

Fig. 7 (a and b) Surface step edge orientation along the $\langle 11\bar{2}0 \rangle$ direction (*A* axis) and along the $\langle 10\bar{1}0 \rangle$ direction (*M* axis) of sapphire (0001), respectively, and the corresponding epitaxial MoS$_2$ domain alignment. (c) The epitaxial relationship of MoS$_2$ on a sapphire (0001) substrate. Black and red arrows indicate the lattice vectors of the sapphire and MoS$_2$, respectively. Schematic of the configuration of the WS$_2$ cluster on a flat *a*-plane sapphire surface for $\theta = 0°$ (d) and 60° (e), where θ is the angle between one zigzag direction of WS$_2$ and the $\langle 1\bar{1}00 \rangle$ plane of the *a*-plane sapphire surface. (f) Binding energy of WS$_2$ triangular islands with *a*-plane sapphire surface at different rotational angles (top panel). Relative energy difference between the antiparallel WS$_2$ islands upon interaction and cross-over of the step-edges in *a*-plane sapphire (bottom panel). (g and h) Calculated distributions of charge difference of the antiparallel ($\theta = 0°$, (g) and 60°, (h) WS$_2$ islands at the step-edges of *a*-plane sapphire. (i) Schematic of WS$_2$ islands grown on *a*-Al$_2$O$_3$ during the early stage of growth. [Fig. 7(a)–(c) are reproduced from Li *et al.*[28] Copyright 2021, rights managed by the Nature Publishing Group. Fig. 7(d)–(i) are reproduced from Wang *et al.*[29] Copyright 2021, rights managed by the Nature Publishing Group].

monolayer MoS$_2$ single crystals film (Fig. 7a–c). Fig. 7a shows that when the step edges are oriented along the $\langle 11\bar{2}0 \rangle$ direction (*A* axis), the step edges become perpendicular to the zigzag (ZZ) edge of the triangular MoS$_2$ domains, which equalizes the two antiparallel domains and prevents the growth of single crystals. Whereas, as shown in Fig. 7b, when the surface step edges are projected along the $\langle 10\bar{1}0 \rangle$ direction (*M* axis), the degeneracy of nucleation energy for antiparallel MoS$_2$ rotational twin domains are lifted, which leads to unidirectional alignment of the MoS$_2$ domains over the 2-inch wafer-scale. Fig. 7c shows the epitaxial relationship of MoS$_2$ on a sapphire (0001) substrate, where black and red arrows indicate the lattice vectors of the sapphire and MoS$_2$, respectively. Wang *et al.* have also recently demonstrated the epitaxial growth of 2-inch single-crystal WS$_2$ monolayer films on vicinal *a*-plane sapphire surfaces (Fig. 7d–i).[29] Fig. 7d and e shows the

schematic of the configuration of the WS$_2$ cluster on a flat *a*-plane sapphire surface for $\theta = 0°$ (Fig. 7d) and 60° (Fig. 7e), where θ is the angle between one zigzag direction of WS$_2$ and the $\langle 1\bar{1}00 \rangle$ plane of the *a*-plane sapphire surface. Top panel of Fig. 7f, shows the binding energy of WS$_2$ triangular islands with the *a*-plane sapphire surface at different rotational angles. Where the binding energy minima reflecting the configurations are shown in Fig. 7d and e. Bottom panel of Fig. 7f, shows the relative energy difference between the antiparallel WS$_2$ islands upon interaction and cross-over of the step-edges in the *a*-plane sapphire surface due to symmetry breaking. Fig. 7g and h show the calculated distributions of charge difference of the antiparallel ($\theta = 0°$ and 60°) WS$_2$ islands at the step-edges of *a*-plane sapphire. This indicates that the binding energy between the step edge and WS$_2$ depends on its alignment and breaks the C_2 symmetry of the WS$_2$/*a*-plane sap-

phire system into C_1, making it possible to have all the WS_2 islands aligned only along one direction, leading to the formation of wafer-scale single crystal upon coalescence (Fig. 7i).

3.3.2. Seed mediated in-plane 2D-epitaxial growth. Although the continuous epitaxial films resulting from the coalescence of orientationally aligned islands have essentially one crystallographic orientation, translational grain boundaries along high-symmetry directions still exist because of the presence of imperfectly coalesced domains.[127,128] Such regions of coalescence sometimes can be located by arrays of metal vacancies in the MC monolayer, leaving behind arrays of point defects.[129] To mitigate this problem, Xu *et al.* devised a seeded 2D epitaxial growth strategy for a 2D-confined single crystal *via* the solid-to-solid phase transition and recrystallization process to produce wafer-scale single crystal films of semiconducting 2H $MoTe_2$ (Fig. 8).[130] Fig. 8a schematically shows the synthesis process, which started from a 10 nm thick polycrystalline 1T′ $MoTe_2$ film having Te vacancies and grain size of about tens of nanometers. Next, a single crystal exfoliated 2H $MoTe_2$ flake was placed at the center of the 1T′ $MoTe_2$ wafer by a dry transfer method, which serves as a seed crystal to initiate the phase transition and recrystallization process.

Since 1T′ $MoTe_2$ is Te deficient, Te atoms were supplied through a hole on 30 nm-thick Al_2O_3 covered 2H $MoTe_2$ flake, to avoid any direct contact between Te and 1T′ $MoTe_2$. This site-specific Te supply pathway induces the 1T′ to 2H $MoTe_2$ phase transition exactly underneath the 2H $MoTe_2$ seed

crystal,[131–133] and simultaneously avoids the spontaneous nucleation of 2H $MoTe_2$ with random crystal orientations in the 1T′ $MoTe_2$ film. With the continuous supply of Te, through the outward transmission of phase transition and recrystallization induced by the vertical 2H/1T′ interface, eventually the 1T′ $MoTe_2$ layer underneath the seed crystal transformed into a wafer-scale 2H $MoTe_2$ single crystal with the same crystallographic orientation as the seed crystal. Fig. 8b shows the OM image of the 2H/1T′ $MoTe_2$ assembly, where a 2H $MoTe_2$ seed nanoflake is placed at the center of the 1T′ $MoTe_2$ wafer. Fig. 8c shows the OM image of the 1T′ $MoTe_2$ wafer at an intermediate growth stage, resulting in a single crystal 2H $MoTe_2$ circle centered on the seed region. The inset shows the seed crystal with a needle probe-punched hole.

3.3.3. Growth *via* surface diffusion and epitaxial self-planarization. State-of-the-art demonstrations of aligned nucleation of 2D MC islands and their seamless stitching at the step-edges of the substrate, to produce single-grain thin films on the wafer-scale, is technologically very challenging to reproduce.[28,29,32] Moreover, upon exposure to high-temperatures (>850 °C), the step-edges tend to distort, resulting in the nucleation of MC domains in various orientations.[127] The prerequisite for the deployment of 2D MC single crystal thin films in industrial applications is the ability to mass-produce them through cost-efficient, reliable, and high-throughput synthesis methods, compatible with the current Si based device fabrication line.[15,17] Apart from the issue of reliable, and high-
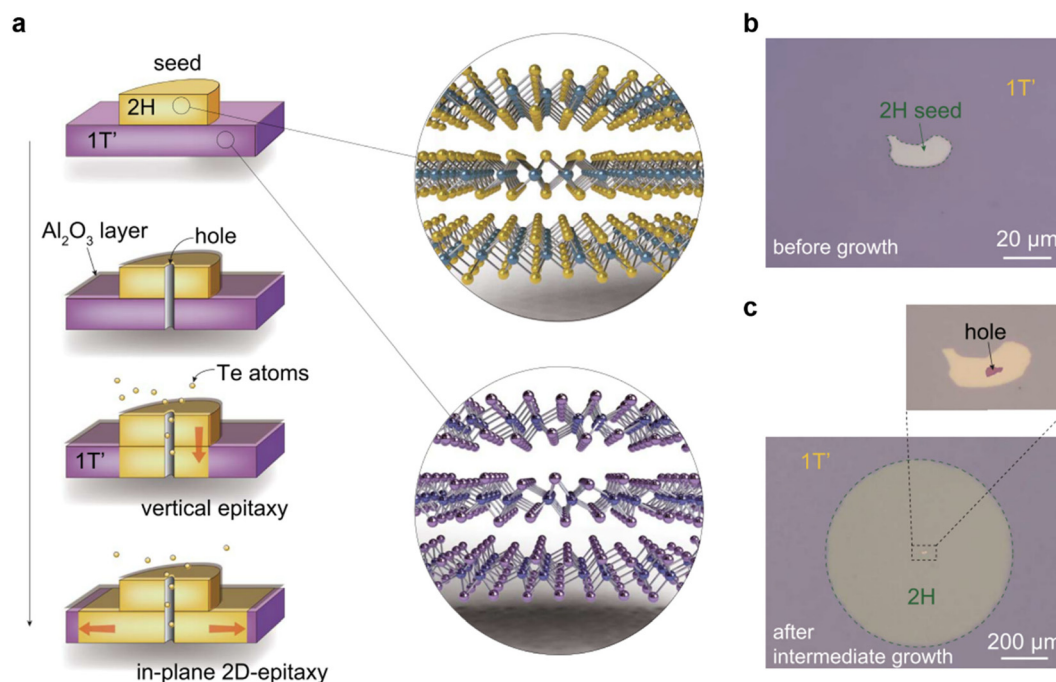

Fig. 8 (a) Schematic illustration showing the in-plane 2D-epitaxy mediated synthesis of a wafer-scale single-crystal 2H-$MoTe_2$ thin film. The 1T′-$MoTe_2$ film on a Si wafer was converted gradually *via* phase transition and recrystallization to the 2H-$MoTe_2$, starting from the hole to the entire area. (b) OM image of a 2H $MoTe_2$ nanoflake assembled in the center of the 1T′ $MoTe_2$ wafer as a seed to induce the phase transition and recrystallization. (c) OM image of the wafer after intermediate growth at 650 °C for 2 hours, where the seed crystal with a needle probe-punched hole is shown in the inset. [Fig. 8 is reproduced with permission from Xu *et al.*[130] Copyright 2021, American Association for the Advancement of Science].

throughput synthesis, the transfer of the MC thin films onto other substrates causes the degradation of the material performance and is not compatible with the device manufacturing lines. Through theoretical calculations and experimental analysis, Giri *et al.* recently demonstrated a generalized synthetic strategy to produce wafer-scale single-crystal MC thin films *via* "surface diffusion and epitaxial self-planarization of randomly oriented grains", to produce wafer-scale single crystal Si_2Te_3, GeTe, GeSe, and GaTe thin films, (Fig. 9).[21] The synthesis used commercial wafers (Si, Ge, GaAs, *etc.*) both as a metal source and an epitaxy collimator. The synthesis is quick and allows atomically smooth single crystal thin films over the entire wafer surface. Fig. 9a–d shows the time dependent SEM images during the growth process of the Si_2Te_3 thin film; Fig. 9(a) shows seed crystal formation from a Te-rich droplet at 630 °C; Fig. (9b) shows growth of small hexagonal crystal domains at 675 °C; Fig. (9c) shows epitaxial self-planarization at 720 °C; and Fig. (9d) shows the formation of the atomically smooth Si_2Te_3 thin film. DFT calculations for single-crystal formation mechanism reveal that chalcogen (Se, Te) diffusion into the wafer substrates (Si, Ge, GaAs, *etc.*) is energetically favorable, and the diffused chalcogens tend to migrate preferentially along the surface of the single crystal wafer substrates and create M_xC_y crystal domains at the surfaces. Under a continuous supply of chalcogens, multiple crystal domains with different thicknesses were formed. Then, due to the high

elemental mobility at the annealing temperature (≥630 °C), surface energy minimization induced self-planarization by viscoelastic lateral translation of the elements, produces an atomically smooth Si_2Te_3 thin film. The epitaxial relationship of the initial M_xC_y crystal domains with the substrate enabled unidirectional alignment of the synthesized thin film; hence, single-crystal thin film formation over the entire substrate was facilitated. The crystal structure of the Si_2Te_3 thin film synthesized at 720 °C for 3 min was characterized by synchrotron X-ray diffraction (XRD). The 2θ XRD pattern of the 35.4 nm-thick Si_2Te_3 film exhibited only $[00l]$ out-of-plane orientations, indicating that all the atomic layers had the same out-of-plane stacking (Fig. 9e). Fig. 9f shows the investigated ϕ scan at different temperatures to identify the mechanism of unidirectional in-plane grain alignment. Where, with increasing the annealing temperature, the population of misaligned domains (indicated with "•") decreases and simultaneously the population of aligned domains increases (indicated with "*"). Finally, all the misaligned domains become aligned with the in-plane substrate peak (Si (220)), upon annealing at 720 °C for 3 min, producing the unidirectionally aligned single crystal Si_2Te_3 thin films on a wafer-scale. Fig. 9g shows the coincidence site lattice (CSL) (dotted triangle) in the interface model between the Te (yellow) layer of Si_2Te_3 and the Si (blue) of Si (111), where the 9-unit mesh of Te coincides with the 10-unit mesh of Si, effectively reducing the lattice mismatch to
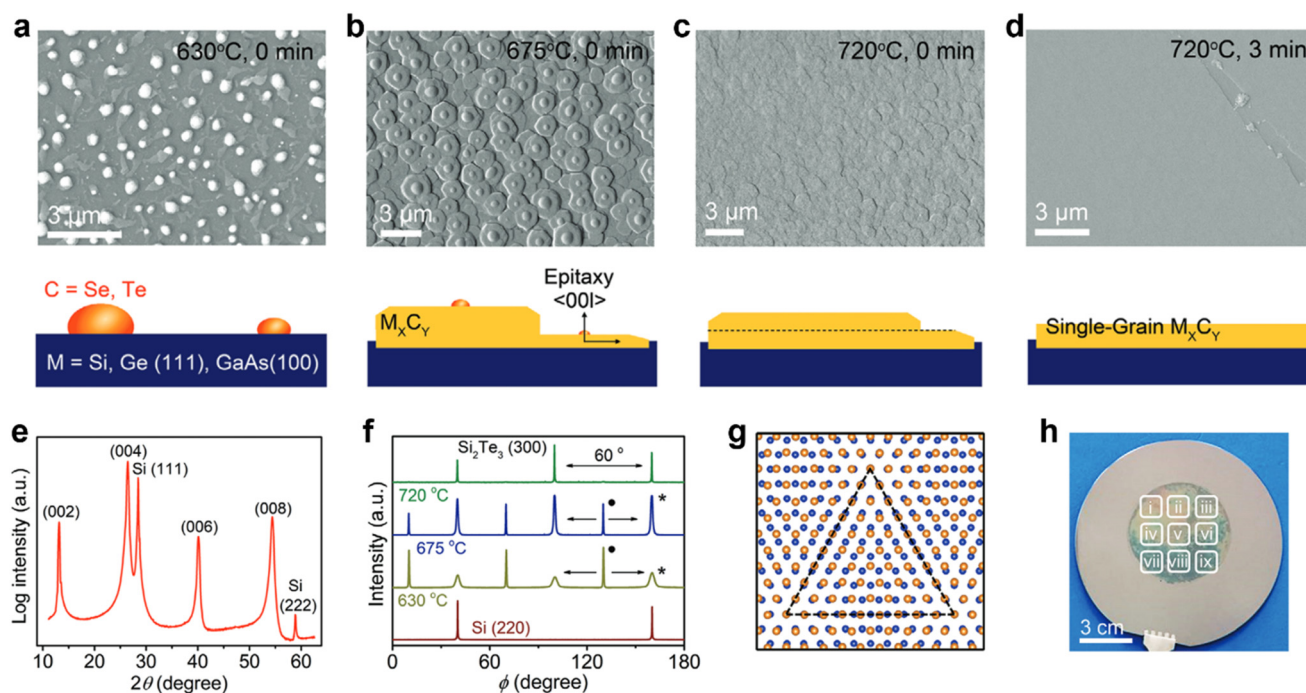

Fig. 9 (a–d) Field emission scanning electron microscopy (FE-SEM) images of the Si_2Te_3 thin film growth process at different temperatures. (e) XRD pattern of the Si_2Te_3 film exhibited only $[00l]$ out-of-plane orientation. (f) Azimuthal φ-scan of the in-plane (300) reflection of Si_2Te_3 at different annealing temperatures. The peak in perfect epitaxial alignment with the Si (220) is indicated by "*" and the peak having 30° mismatch with Si (220) is indicated with "•". (g) The coincidence site lattice (CSL) (dotted triangle) in the interface model between the Te (yellow) layer of Si_2Te_3 and Si (blue) of Si (111). (h) Digital image of 2-inch single-grain Si_2Te_3 thin film grown on the 4-inch Si (111) wafer. [Fig. 9 is adopted with permission from Giri *et al.*[21] Copyright 2021, Wiley-VCH, Weinheim].

+0.54%, and providing perfect epitaxial growth conditions for wafer-scale (2-inch) single crystal Si_2Te_3 thin film growth on the 4-inch Si (111) wafer (Fig. 9h).

4. Conclusion and outlook

The novel properties[4,134,135] and promising applications[4,136-138] of 2D vdW materials have motivated increasing attempts to synthesize high quality 2D vdW thin films since monolayer graphene was prepared.[139-141] To realize their industrial applications, which is the ultimate goal, it is of paramount importance to have readily available wafer-scale single crystal thin films of 2D vdW materials.[14,15] Although the nucleation-controlled growth by suppressing the nucleation density is an effective strategy to produce large-scale single crystal graphene,[65] due to its lower growth rate it takes several hours to grow a fully covered wafer-scale graphene film. Nevertheless, because of the complicated experimental design and the sensitivity of the process to control gas flow in the reactor, the process is not cost-effective and inconvenient. In contrast, unidirectional alignment of multiple epitaxial nuclei and their seamless coalescence into a large-area single crystal graphene, have several advantages including shorter growth time and require lesser stringent growth conditions.[74] Recent successful growth of wafer-scale single crystal graphene mono-layers directly on electrically insulating Al_2O_3 (0001) wafers could also contribute to next-generation graphene-based nanodevices.[27]

Recent studies have shown the growth of single crystal hBN films on molten gold surfaces or bulk Cu or Ni foils.[19,20,24] However, the use of molten gold is not favored by industry, owing to its high cost, cross-contamination and potential issues of process control and scalability. Copper foils might be suitable for roll-to-roll processes but are unlikely to be compatible with advanced microelectronic fabrication on wafers. However, the successful epitaxial growth of 2-inch single-crystal hBN monolayers on a Cu (111) thin film deposited over c-plane sapphire wafer is a reliable approach to produce wafer-scale single-crystal hBN and paves the way to future 2D electronics.[22] More studies are needed on the synthesis of multi-layer hBN on low-symmetry single crystalline substrates in the future.

The recent successful synthesis of wafer-scale single crystal MoS_2 and WS_2 monolayers on Al_2O_3 surfaces with periodic step-edges boosted research interest in synthesizing wafer-scale 2D vdW MC thin films where the microstructure and uni-directional nature of the monolayer are attributed to the high nucleation density along the sapphire surface steps and their seamless coalescence of the aligned domains. However, the production of the well-aligned step-edges is technologically very challenging to reproduce.[28,29,32] Moreover, upon high-temperature (>850 °C) exposure, the step-edges tend to distort, resulting in the nucleation of MC domains in various orientations.[127] Growth conditions that preserve the aligned step-edge morphology while promoting surface diffusion and lateral domain growth are necessary to reduce domain mis-orientation and achieve unidirectional growth. In this regard, the generalized epitaxial synthetic concept, viz. "surface diffusion and epitaxial self-planarization", for the production of wafer-scale single crystal metal chalcogenide thin films (Si_2Te_3, GeTe, GeSe, and GaTe) directly on commercial wafers (Si, Ge, GaAs, etc.) and their utilization in the transfer-free fabrication of devices, is believed to open a new technological window for both the 2D vdW wafer-scale single crystal synthesis and the device fabrication process.[21] Although the continuous epitaxial films resulting from the coalescence of orientationally aligned islands have essentially one crystallographic orientation, translational grain boundaries along high-symmetry directions still exist because of the presence of imperfectly coalesced domains.[127,128] Such regions of coalescence sometimes can be located by arrays of metal vacancies in the MC monolayer, leaving behind arrays of point defects.[129] A recently developed method of seeded 2D epitaxial growth of a wafer-scale single crystal film of semiconducting 2H $MoTe_2$ via solid-to-solid phase transition and recrystallization processes, mitigates this issue of imperfect coalescence,[130] which can be used as a template for further rapid epitaxy in a vertical manner.

Although recently several epitaxial growth strategies of wafer-scale 2D vdW single-crystal films have been demonstrated, the industrial scale production of 2D materials is still a big challenge, especially compared to chip-grade single-crystal silicon. One problem is how to grow single crystal 2D vdW materials with high uniformity and excellent electrical properties on a wafer scale. Currently, the main method of growing single crystal thin films is to control the uni-directional orientation of the crystal domains to allow their seamless coalescence and stitching. However, the continuous epitaxial films resulting from the coalescence of orientation-ally aligned islands are also expected to exhibit facets along high-symmetry directions.[128] Moreover, translational defect arrays and grain boundaries still exist in a nearly single-orientation, coalesced monolayer 2D vdW film due to the presence of imperfectly stitched domains.[127-129] These defective grain boundaries in 2D semiconductors usually exhibit metallic characteristics and serve as conducting channels, seriously impairing the electrical and optical properties of related devices. Therefore, connecting atomic-scale defects to larger morphologies poses a significant challenge. Additionally, it has been difficult to control the nucleation of 2D materials to get a unidirectionally aligned multilayer single-crystal 2D vdW film on the wafer scale. The indefinite kinetic control of the layer-by-layer growth of 2D vdW materials arises due to the complexity of the precursor species and their gradient feeding distributions along the gas flow direction. Also, currently the synthesized 2D vdW thin films need to be transferred from the growth substrate to the target substrate for device fabrication. However, the traditional transfer process can damage the grown films, due to the formation of wrinkles, cracks, and polymer contamination, seriously affecting the device performance of the synthesized 2D vdW thin films.

Finally, the technique for the mass production of wafer-scale single crystal 2D vdW materials must be able to provide the required quantities while ensuring reliable quality for industrial-scale applications. The development of a reliable large-scale production process, with special emphasis on quality, cost, reproducibility, processability and safety, would not only unleash the potential of 2D vdW materials in electronic and optoelectronic applications, but may also help trigger other key applications, where the unique properties of 2D vdW materials can produce significant enhancements. However, the growth model of 2D vdW materials is far from complete and further attention and efforts are required, including increasing precursor supply, local feeding of precursors, and reduction of pre-deposited transition metal containing thin films, to elucidate the growth mechanism of wafer-scale single crystal 2D vdW materials.

Conflicts of interest

There are no conflicts to declare.

Acknowledgements

References

1 K. S. Novoselov, A. Mishchenko, A. Carvalho and A. H. Castro Neto, *Science*, 2016, **353**, aac9439.

2 K. F. Mak, C. Lee, J. Hone, J. Shan and T. F. Heinz, *Phys. Rev. Lett.*, 2010, **105**, 136805.

3 M. Xu, T. Liang, M. Shi and H. Chen, *Chem. Rev.*, 2013, **113**, 3766–3798.

4 A. Giri, G. Park and U. Jeong, *Chem. Rev.*, 2023, **123**, 3329–3442.

5 M. C. Lemme, D. Akinwande, C. Huyghebaert and C. Stampfer, *Nat. Commun.*, 2022, **13**, 1392.

6 M. Zeng, Y. Xiao, J. Liu, K. Yang and L. Fu, *Chem. Rev.*, 2018, **118**, 6236–6296.

7 F. Xia, H. Wang, D. Xiao, M. Dubey and A. Ramasubramaniam, *Nat. Photonics*, 2014, **8**, 899–907.

8 W. Miao, L. Wang, X. Mu and J. Wang, *J. Mater. Chem. C*, 2021, **9**, 13600–13616.

9 L. J. Li, E. C. T. O'Farrell, K. P. Loh, G. Eda, B. Özyilmaz and A. H. Castro Neto, *Nature*, 2016, **529**, 185–189.

10 C. Tőke and V. I. Fal'ko, *Phys. Rev. B: Condens. Matter Mater. Phys.*, 2014, **90**, 035404.

11 J. T. Ye, Y. J. Zhang, R. Akashi, M. S. Bahramy, R. Arita and Y. Iwasa, *Science*, 2012, **338**, 1193–1196.

12 J. M. Park, Y. Cao, L.-Q. Xia, S. Sun, K. Watanabe, T. Taniguchi and P. Jarillo-Herrero, *Nat. Mater.*, 2022, **21**, 877–883.

13 Y. Cao, V. Fatemi, S. Fang, K. Watanabe, T. Taniguchi, E. Kaxiras and P. Jarillo-Herrero, *Nature*, 2018, **556**, 43–50.

14 D. Neumaier, S. Pindl and M. C. Lemme, *Nat. Mater.*, 2019, **18**, 525–529.

15 V. Dusastre, *Nat. Mater.*, 2019, **18**, 519–519.

16 L. Lin, H. Peng and Z. Liu, *Nat. Mater.*, 2019, **18**, 520–524.

17 A. K. Singh, B. Thakurta, A. Giri and M. Pal, *Chem. Commun.*, 2024, **60**, 265–279.

18 J. Zhou, J. Lin, X. Huang, Y. Zhou, Y. Chen, J. Xia, H. Wang, Y. Xie, H. Yu, J. Lei, D. Wu, F. Liu, Q. Fu, Q. Zeng, C.-H. Hsu, C. Yang, L. Lu, T. Yu, Z. Shen, H. Lin, B. I. Yakobson, Q. Liu, K. Suenaga, G. Liu and Z. Liu, *Nature*, 2018, **556**, 355–359.

19 L. Wang, X. Xu, L. Zhang, R. Qiao, M. Wu, Z. Wang, S. Zhang, J. Liang, Z. Zhang, Z. Zhang, W. Chen, X. Xie, J. Zong, Y. Shan, Y. Guo, M. Willinger, H. Wu, Q. Li, W. Wang, P. Gao, S. Wu, Y. Zhang, Y. Jiang, D. Yu, E. Wang, X. Bai, Z.-J. Wang, F. Ding and K. Liu, *Nature*, 2019, **570**, 91–95.

20 J. S. Lee, S. H. Choi, S. J. Yun, Y. I. Kim, S. Boandoh, J.-H. Park, B. G. Shin, H. Ko, S. H. Lee, Y.-M. Kim, Y. H. Lee, K. K. Kim and S. M. Kim, *Science*, 2018, **362**, 817–821.

21 A. Giri, M. Kumar, J. Kim, M. Pal, W. Banerjee, R. D. Nikam, J. Kwak, M. Kong, S. H. Kim, K. Thiyagarajan, G. Kim, H. Hwang, H. H. Lee, D. Lee and U. Jeong, *Adv. Mater.*, 2021, **33**, 2102252.

22 T.-A. Chen, C.-P. Chuu, C.-C. Tseng, C.-K. Wen, H. S. P. Wong, S. Pan, R. Li, T.-A. Chao, W.-C. Chueh, Y. Zhang, Q. Fu, B. I. Yakobson, W.-H. Chang and L.-J. Li, *Nature*, 2020, **579**, 219–223.

23 D. Luo, M. Wang, Y. Li, C. Kim, K. M. Yu, Y. Kim, H. Han, M. Biswal, M. Huang, Y. Kwon, M. Goo, D. C. Camacho-Mojica, H. Shi, W. J. Yoo, M. S. Altman, H.-J. Shin and R. S. Ruoff, *Adv. Mater.*, 2019, **31**, 1903615.

24 K. Y. Ma, L. Zhang, S. Jin, Y. Wang, S. I. Yoon, H. Hwang, J. Oh, D. S. Jeong, M. Wang, S. Chatterjee, G. Kim, A. R. Jang, J. Yang, S. Ryu, H. Y. Jeong, R. S. Ruoff, M. Chhowalla, F. Ding and H. S. Shin, *Nature*, 2022, **606**, 88–93.

25 M. Wang, M. Huang, D. Luo, Y. Li, M. Choe, W. K. Seong, M. Kim, S. Jin, M. Wang, S. Chatterjee, Y. Kwon, Z. Lee and R. S. Ruoff, *Nature*, 2021, **596**, 519–524.

26 J.-H. Lee, E. K. Lee, W.-J. Joo, Y. Jang, B.-S. Kim, J. Y. Lim, S.-H. Choi, S. J. Ahn, J. R. Ahn, M.-H. Park, C.-W. Yang, B. L. Choi, S.-W. Hwang and D. Whang, *Science*, 2014, **344**, 286–289.

27 J. Li, M. Chen, A. Samad, H. Dong, A. Ray, J. Zhang, X. Jiang, U. Schwingenschlögl, J. Domke, C. Chen, Y. Han, T. Fritz, R. S. Ruoff, B. Tian and X. Zhang, *Nat. Mater.*, 2022, **21**, 740–747.

28 T. Li, W. Guo, L. Ma, W. Li, Z. Yu, Z. Han, S. Gao, L. Liu, D. Fan, Z. Wang, Y. Yang, W. Lin, Z. Luo, X. Chen, N. Dai,

X. Tu, D. Pan, Y. Yao, P. Wang, Y. Nie, J. Wang, Y. Shi and X. Wang, *Nat. Nanotechnol.*, 2021, **16**, 1201–1207.

29 J. Wang, X. Xu, T. Cheng, L. Gu, R. Qiao, Z. Liang, D. Ding, H. Hong, P. Zheng, Z. Zhang, Z. Zhang, S. Zhang, G. Cui, C. Chang, C. Huang, J. Qi, J. Liang, C. Liu, Y. Zuo, G. Xue, X. Fang, J. Tian, M. Wu, Y. Guo, Z. Yao, Q. Jiao, L. Liu, P. Gao, Q. Li, R. Yang, G. Zhang, Z. Tang, D. Yu, E. Wang, J. Lu, Y. Zhao, S. Wu, F. Ding and K. Liu, *Nat. Nanotechnol.*, 2022, **17**, 33–38.

30 A. Aljarb, J.-H. Fu, C.-C. Hsu, C.-P. Chuu, Y. Wan, M. Hakami, D. R. Naphade, E. Yengel, C.-J. Lee, S. Brems, T.-A. Chen, M.-Y. Li, S.-H. Bae, W.-T. Hsu, Z. Cao, R. Albaridy, S. Lopatin, W.-H. Chang, T. D. Anthopoulos, J. Kim, L.-J. Li and V. Tung, *Nat. Mater.*, 2020, **19**, 1300–1306.

31 S. H. Choi, H.-J. Kim, B. Song, Y. I. Kim, G. Han, H. T. T. Nguyen, H. Ko, S. Boandoh, J. H. Choi, C. S. Oh, H. J. Cho, J. W. Jin, Y. S. Won, B. H. Lee, S. J. Yun, B. G. Shin, H. Y. Jeong, Y.-M. Kim, Y.-K. Han, Y. H. Lee, S. M. Kim and K. K. Kim, *Adv. Mater.*, 2021, **33**, 2006601.

32 P. Yang, S. Zhang, S. Pan, B. Tang, Y. Liang, X. Zhao, Z. Zhang, J. Shi, Y. Huan, Y. Shi, S. J. Pennycook, Z. Ren, G. Zhang, Q. Chen, X. Zou, Z. Liu and Y. Zhang, *ACS Nano*, 2020, **14**, 5036–5045.

33 Z. Sun, Z. Yan, J. Yao, E. Beitler, Y. Zhu and J. M. Tour, *Nature*, 2010, **468**, 549–552.

34 X. Yang, Z. Guan, M. Zeng, J. Wei, W. Wang and X. Bai, *Small*, 2013, **9**, 1353–1358.

35 K.-K. Liu, W. Zhang, Y.-H. Lee, Y.-C. Lin, M.-T. Chang, C.-Y. Su, C.-S. Chang, H. Li, Y. Shi, H. Zhang, C.-S. Lai and L.-J. Li, *Nano Lett.*, 2012, **12**, 1538–1544.

36 M. J. Allen, V. C. Tung and R. B. Kaner, *Chem. Rev.*, 2010, **110**, 132–145.

37 K. S. Novoselov, V. I. Fal'ko, L. Colombo, P. R. Gellert, M. G. Schwab and K. Kim, *Nature*, 2012, **490**, 192–200.

38 L. Zhang, J. Dong and F. Ding, *Chem. Rev.*, 2021, **121**, 6321–6372.

39 A. Giri, G. Park, H. Yang, M. Pal, J. Kwak and U. Jeong, *Adv. Mater.*, 2018, **30**, 1707577.

40 G. H. Han, D. L. Duong, D. H. Keum, S. J. Yun and Y. H. Lee, *Chem. Rev.*, 2018, **118**, 6297–6336.

41 Z. Cai, B. Liu, X. Zou and H.-M. Cheng, *Chem. Rev.*, 2018, **118**, 6091–6133.

42 H. Lin, Z. Zhang, H. Zhang, K.-T. Lin, X. Wen, Y. Liang, Y. Fu, A. K. T. Lau, T. Ma, C.-W. Qiu and B. Jia, *Chem. Rev.*, 2022, **122**, 15204–15355.

43 C. Dai, Y. Liu and D. Wei, *Chem. Rev.*, 2022, **122**, 10319–10392.

44 D. Steiner, M. Thaler, T. Mairegger, F. Mittendorfer and E. Bertel, *J. Phys. Chem. C*, 2023, **127**, 11559–11569.

45 M. S. Islam, A. A. M. Mazumder, M. U. Sohag, M. M. H. Sarkar, C. Stampfl and J. Park, *Nanoscale Adv.*, 2023, **5**, 4041–4064.

46 Y. Liu, A. Dobrinsky and B. I. Yakobson, *Phys. Rev. Lett.*, 2010, **105**, 235502.

47 V. I. Artyukhov, Y. Liu and B. I. Yakobson, *Proc. Natl. Acad. Sci. U. S. A.*, 2012, **109**, 15136–15140.

48 H. Shu, X. Chen, X. Tao and F. Ding, *ACS Nano*, 2012, **6**, 3243–3250.

49 T. Ma, W. Ren, X. Zhang, Z. Liu, Y. Gao, L.-C. Yin, X.-L. Ma, F. Ding and H.-M. Cheng, *Proc. Natl. Acad. Sci. U. S. A.*, 2013, **110**, 20386–20391.

50 X. Li, J. Dong, J. C. Idrobo, A. A. Puretzky, C. M. Rouleau, D. B. Geohegan, F. Ding and K. Xiao, *J. Am. Chem. Soc.*, 2017, **139**, 482–491.

51 Z. Zhang, Y. Liu, Y. Yang and B. I. Yakobson, *Nano Lett.*, 2016, **16**, 1398–1403.

52 T. Zhao, J. Guo, T. Li, Z. Wang, M. Peng, F. Zhong, Y. Chen, Y. Yu, T. Xu, R. Xie, P. Gao, X. Wang and W. Hu, *Chem. Soc. Rev.*, 2023, **52**, 1650–1671.

53 G. Kim, D. Kim, Y. Choi, A. Ghorai, G. Park and U. Jeong, *Adv. Mater.*, 2023, **35**, 2203373.

54 J. Singh, N. A. Astarini, M.-L. Tsai, M. Venkatesan, C.-C. Kuo, C.-S. Yang and H.-W. Yen, *Adv. Sci.*, 2024, 2307839, n/a.

55 J. Gao, J. Zhao and F. Ding, *J. Am. Chem. Soc.*, 2012, **134**, 6204–6209.

56 J. Gao, J. Yip, J. Zhao, B. I. Yakobson and F. Ding, *J. Am. Chem. Soc.*, 2011, **133**, 5009–5015.

57 A. T. Murdock, A. Koos, T. B. Britton, L. Houben, T. Batten, T. Zhang, A. J. Wilkinson, R. E. Dunin-Borkowski, C. E. Lekka and N. Grobert, *ACS Nano*, 2013, **7**, 1351–1359.

58 W. Ma, M.-L. Chen, L. Yin, Z. Liu, H. Li, C. Xu, X. Xin, D.-M. Sun, H.-M. Cheng and W. Ren, *Nat. Commun.*, 2019, **10**, 2809.

59 J. Dong, L. Zhang, X. Dai and F. Ding, *Nat. Commun.*, 2020, **11**, 5862.

60 M. Huang, M. Biswal, H. J. Park, S. Jin, D. Qu, S. Hong, Z. Zhu, L. Qiu, D. Luo, X. Liu, Z. Yang, Z. Liu, Y. Huang, H. Lim, W. J. Yoo, F. Ding, Y. Wang, Z. Lee and R. S. Ruoff, *ACS Nano*, 2018, **12**, 6117–6127.

61 X. Song, J. Gao, Y. Nie, T. Gao, J. Sun, D. Ma, Q. Li, Y. Chen, C. Jin, A. Bachmatiuk, M. H. Rümmeli, F. Ding, Y. Zhang and Z. Liu, *Nano Res.*, 2015, **8**, 3164–3176.

62 X. Li, W. Cai, J. An, S. Kim, J. Nah, D. Yang, R. Piner, A. Velamakanni, I. Jung, E. Tutuc, S. K. Banerjee, L. Colombo and R. S. Ruoff, *Science*, 2009, **324**, 1312–1314.

63 I. V. Vlassiouk, Y. Stehle, P. R. Pudasaini, R. R. Unocic, P. D. Rack, A. P. Baddorf, I. N. Ivanov, N. V. Lavrik, F. List, N. Gupta, K. V. Bets, B. I. Yakobson and S. N. Smirnov, *Nat. Mater.*, 2018, **17**, 318–322.

64 B. Deng, Z. Liu and H. Peng, *Adv. Mater.*, 2019, **31**, 1800996.

65 T. Wu, X. Zhang, Q. Yuan, J. Xue, G. Lu, Z. Liu, H. Wang, H. Wang, F. Ding, Q. Yu, X. Xie and M. Jiang, *Nat. Mater.*, 2016, **15**, 43–47.

66 Q. Yu, L. A. Jauregui, W. Wu, R. Colby, J. Tian, Z. Su, H. Cao, Z. Liu, D. Pandey, D. Wei, T. F. Chung, P. Peng, N. P. Guisinger, E. A. Stach, J. Bao, S.-S. Pei and Y. P. Chen, *Nat. Mater.*, 2011, **10**, 443–449.

67 L. Liu, H. Zhou, R. Cheng, Y. Chen, Y.-C. Lin, Y. Qu, J. Bai, I. A. Ivanov, G. Liu, Y. Huang and X. Duan, *J. Mater. Chem.*, 2012, **22**, 1498–1503.

68 H. Wang, G. Wang, P. Bao, S. Yang, W. Zhu, X. Xie and W.-J. Zhang, *J. Am. Chem. Soc.*, 2012, **134**, 3627–3630.

69 Z. Yan, J. Lin, Z. Peng, Z. Sun, Y. Zhu, L. Li, C. Xiang, E. L. Samuel, C. Kittrell and J. M. Tour, *ACS Nano*, 2012, **6**, 9110–9117.

70 Y. Hao, M. S. Bharathi, L. Wang, Y. Liu, H. Chen, S. Nie, X. Wang, H. Chou, C. Tan, B. Fallahazad, H. Ramanarayan, C. W. Magnuson, E. Tutuc, B. I. Yakobson, K. F. McCarty, Y.-W. Zhang, P. Kim, J. Hone, L. Colombo and R. S. Ruoff, *Science*, 2013, **342**, 720–723.

71 Y. Hao, L. Wang, Y. Liu, H. Chen, X. Wang, C. Tan, S. Nie, J. W. Suk, T. Jiang, T. Liang, J. Xiao, W. Ye, C. R. Dean, B. I. Yakobson, K. F. McCarty, P. Kim, J. Hone, L. Colombo and R. S. Ruoff, *Nat. Nanotechnol.*, 2016, **11**, 426–431.

72 L. Lin, L. Sun, J. Zhang, J. Sun, A. L. Koh, H. Peng and Z. Liu, *Adv. Mater.*, 2016, **28**, 4671–4677.

73 H. Wang, X. Xu, J. Li, L. Lin, L. Sun, X. Sun, S. Zhao, C. Tan, C. Chen, W. Dang, H. Ren, J. Zhang, B. Deng, A. L. Koh, L. Liao, N. Kang, Y. Chen, H. Xu, F. Ding, K. Liu, H. Peng and Z. Liu, *Adv. Mater.*, 2016, **28**, 8968–8974.

74 X. Sun, L. Lin, L. Sun, J. Zhang, D. Rui, J. Li, M. Wang, C. Tan, N. Kang, D. Wei, H. Q. Xu, H. Peng and Z. Liu, *Small*, 2018, **14**, 1702916.

75 D. Ding, P. Solís-Fernández, H. Hibino and H. Ago, *ACS Nano*, 2016, **10**, 11196–11204.

76 H. Zhou, W. J. Yu, L. Liu, R. Cheng, Y. Chen, X. Huang, Y. Liu, Y. Wang, Y. Huang and X. Duan, *Nat. Commun.*, 2013, **4**, 2096.

77 X. Li, C. W. Magnuson, A. Venugopal, R. M. Tromp, J. B. Hannon, E. M. Vogel, L. Colombo and R. S. Ruoff, *J. Am. Chem. Soc.*, 2011, **133**, 2816–2819.

78 S. Chen, H. Ji, H. Chou, Q. Li, H. Li, J. W. Suk, R. Piner, L. Liao, W. Cai and R. S. Ruoff, *Adv. Mater.*, 2013, **25**, 2062–2065.

79 S. M. Kim, A. Hsu, Y.-H. Lee, M. Dresselhaus, T. Palacios, K. K. Kim and J. Kong, *Nanotechnology*, 2013, **24**, 365602.

80 N. Reckinger, X. Tang, F. Joucken, L. Lajaunie, R. Arenal, E. Dubois, B. Hackens, L. Henrard and J.-F. Colomer, *Nanoscale*, 2016, **8**, 18751–18759.

81 A. Ibrahim, G. Nadhreen, S. Akhtar, F. M. Kafiah and T. Laoui, *Carbon*, 2017, **123**, 402–414.

82 H. K. Yu, K. Balasubramanian, K. Kim, J.-L. Lee, M. Maiti, C. Ropers, J. Krieg, K. Kern and A. M. Wodtke, *ACS Nano*, 2014, **8**, 8636–8643.

83 W. Liu, H. Li, C. Xu, Y. Khatami and K. Banerjee, *Carbon*, 2011, **49**, 4122–4130.

84 M.-S. Won, O. V. Penkov and D.-E. Kim, *Carbon*, 2013, **54**, 472–481.

85 M. H. Griep, T. M. Tumlin, J. T. Smith, S. Oida, T. Sano, D. Demaree and C. Dimitrakopoulos, *Cryst. Growth Des.*, 2017, **17**, 5725–5731.

86 Y. Pan, Y. Liu, X. Lu, G. Pan and J. Luo, *J. Electrochem. Soc.*, 2012, **159**, H329.

87 L. Gan and Z. Luo, *ACS Nano*, 2013, **7**, 9480–9488.

88 W. Guo, F. Jing, J. Xiao, C. Zhou, Y. Lin and S. Wang, *Adv. Mater.*, 2016, **28**, 3152–3158.

89 L. Lin, J. Li, H. Ren, A. L. Koh, N. Kang, H. Peng, H. Q. Xu and Z. Liu, *ACS Nano*, 2016, **10**, 2922–2929.

90 H. Ren, H. Wang, L. Lin, M. Tang, S. Zhao, B. Deng, M. K. Priydarshi, J. Zhang, H. Peng and Z. Liu, *Nano Res.*, 2017, **10**, 1189–1199.

91 T. Ma, W. Ren, Z. Liu, L. Huang, L.-P. Ma, X. Ma, Z. Zhang, L.-M. Peng and H.-M. Cheng, *ACS Nano*, 2014, **8**, 12806–12813.

92 J. Dai, D. Wang, M. Zhang, T. Niu, A. Li, M. Ye, S. Qiao, G. Ding, X. Xie, Y. Wang, P. K. Chu, Q. Yuan, Z. Di, X. Wang, F. Ding and B. I. Yakobson, *Nano Lett.*, 2016, **16**, 3160–3165.

93 X. Xu, Z. Zhang, J. Dong, D. Yi, J. Niu, M. Wu, L. Lin, R. Yin, M. Li, J. Zhou, S. Wang, J. Sun, X. Duan, P. Gao, Y. Jiang, X. Wu, H. Peng, R. S. Ruoff, Z. Liu, D. Yu, E. Wang, F. Ding and K. Liu, *Sci. Bull.*, 2017, **62**, 1074–1080.

94 M. Gao, Y. Pan, L. Huang, H. Hu, L. Z. Zhang, H. M. Guo, S. X. Du and H.-J. Gao, *Appl. Phys. Lett.*, 2011, **98**, 033101.

95 T. Gao, S. Xie, Y. Gao, M. Liu, Y. Chen, Y. Zhang and Z. Liu, *ACS Nano*, 2011, **5**, 9194–9201.

96 L. Gao, W. Ren, H. Xu, L. Jin, Z. Wang, T. Ma, L.-P. Ma, Z. Zhang, Q. Fu, L.-M. Peng, X. Bao and H.-M. Cheng, *Nat. Commun.*, 2012, **3**, 699.

97 H. Kang, P. Tang, H. Shu, Y. Zhang, Y. Liang, J. Li, Z. Chen, Y. Sui, S. Hu, S. Wang, S. Zhao, X. Zhang, C. Jiang, Y. Chen, Z. Xue, M. Zhang, D. Jiang, G. Yu, S. Peng, Z. Jin and X. Liu, *Carbon*, 2021, **181**, 225–233.

98 O. T. Ogurtani, D. Senyildiz and G. Cambaz Buke, *Surf. Interface Anal.*, 2018, **50**, 547–551.

99 X. Zhang, T. Wu, Q. Jiang, H. Wang, H. Zhu, Z. Chen, R. Jiang, T. Niu, Z. Li, Y. Zhang, Z. Qiu, G. Yu, A. Li, S. Qiao, H. Wang, Q. Yu and X. Xie, *Small*, 2019, **15**, 1805395.

100 H. Chen, W. Zhu and Z. Zhang, *Phys. Rev. Lett.*, 2010, **104**, 186101.

101 Q. Yuan, B. I. Yakobson and F. Ding, *J. Phys. Chem. Lett.*, 2014, **5**, 3093–3099.

102 D. Usachov, A. M. Dobrotvorskii, A. Varykhalov, O. Rader, W. Gudat, A. M. Shikin and V. K. Adamchuk, *Phys. Rev. B: Condens. Matter Mater. Phys.*, 2008, **78**, 085403.

103 P. Sutter, J. T. Sadowski and E. Sutter, *Phys. Rev. B: Condens. Matter Mater. Phys.*, 2009, **80**, 245411.

104 S.-Y. Kwon, C. V. Ciobanu, V. Petrova, V. B. Shenoy, J. Bareño, V. Gambin, I. Petrov and S. Kodambaka, *Nano Lett.*, 2009, **9**, 3985–3990.

105 J. Coraux, A. T. N'Diaye, C. Busse and T. Michely, *Nano Lett.*, 2008, **8**, 565–570.

106 B. Wang, X. Ma, M. Caffio, R. Schaub and W.-X. Li, *Nano Lett.*, 2011, **11**, 424–430.

107 L. Wang, B. Wu, J. Chen, H. Liu, P. Hu and Y. Liu, *Adv. Mater.*, 2014, **26**, 1559–1564.

108 R. Y. Tay, M. H. Griep, G. Mallick, S. H. Tsang, R. S. Singh, T. Tumlin, E. H. T. Teo and S. P. Karna, *Nano Lett.*, 2014, **14**, 839–846.

109 R. Y. Tay, X. Wang, S. H. Tsang, G. C. Loh, R. S. Singh, H. Li, G. Mallick and E. H. Tong Teo, *J. Mater. Chem. C*, 2014, **2**, 1650–1657.

110 A. Ismach, H. Chou, D. A. Ferrer, Y. Wu, S. McDonnell, H. C. Floresca, A. Covacevich, C. Pope, R. Piner, M. J. Kim, R. M. Wallace, L. Colombo and R. S. Ruoff, *ACS Nano*, 2012, **6**, 6378–6385.

111 Y. Shi, C. Hamsen, X. Jia, K. K. Kim, A. Reina, M. Hofmann, A. L. Hsu, K. Zhang, H. Li, Z.-Y. Juang, M. S. Dresselhaus, L.-J. Li and J. Kong, *Nano Lett.*, 2010, **10**, 4134–4139.

112 G. Kim, A. R. Jang, H. Y. Jeong, Z. Lee, D. J. Kang and H. S. Shin, *Nano Lett.*, 2013, **13**, 1834–1839.

113 Y. Gao, W. Ren, T. Ma, Z. Liu, Y. Zhang, W.-B. Liu, L.-P. Ma, X. Ma and H.-M. Cheng, *ACS Nano*, 2013, **7**, 5199–5206.

114 P. Sutter, J. Lahiri, P. Albrecht and E. Sutter, *ACS Nano*, 2011, **5**, 7303–7309.

115 N. Guo, J. Wei, L. Fan, Y. Jia, D. Liang, H. Zhu, K. Wang and D. Wu, *Nanotechnology*, 2012, **23**, 415605.

116 A. G. F. Garcia, M. Neumann, F. Amet, J. R. Williams, K. Watanabe, T. Taniguchi and D. Goldhaber-Gordon, *Nano Lett.*, 2012, **12**, 4449–4454.

117 A. L. Gibb, N. Alem, J.-H. Chen, K. J. Erickson, J. Ciston, A. Gautam, M. Linck and A. Zettl, *J. Am. Chem. Soc.*, 2013, **135**, 6758–6761.

118 O. Cretu, Y.-C. Lin and K. Suenaga, *Nano Lett.*, 2014, **14**, 1064–1068.

119 B. E. Feldman, J. Martin and A. Yacoby, *Nat. Phys.*, 2009, **5**, 889–893.

120 D. Geng, B. Wu, Y. Guo, L. Huang, Y. Xue, J. Chen, G. Yu, L. Jiang, W. Hu and Y. Liu, *Proc. Natl. Acad. Sci. U. S. A.*, 2012, **109**, 7992–7996.

121 Y.-H. Chang, W. Zhang, Y. Zhu, Y. Han, J. Pu, J.-K. Chang, W.-T. Hsu, J.-K. Huang, C.-L. Hsu, M.-H. Chiu, T. Takenobu, H. Li, C.-I. Wu, W.-H. Chang, A. T. S. Wee and L.-J. Li, *ACS Nano*, 2014, **8**, 8582–8590.

122 J.-K. Huang, J. Pu, C.-L. Hsu, M.-H. Chiu, Z.-Y. Juang, Y.-H. Chang, W.-H. Chang, Y. Iwasa, T. Takenobu and L.-J. Li, *ACS Nano*, 2014, **8**, 923–930.

123 X. Sang, X. Li, W. Zhao, J. Dong, C. M. Rouleau, D. B. Geohegan, F. Ding, K. Xiao and R. R. Unocic, *Nat. Commun.*, 2018, **9**, 2051.

124 Q. Ji, M. Kan, Y. Zhang, Y. Guo, D. Ma, J. Shi, Q. Sun, Q. Chen, Y. Zhang and Z. Liu, *Nano Lett.*, 2015, **15**, 198–205.

125 H. Yu, M. Liao, W. Zhao, G. Liu, X. J. Zhou, Z. Wei, X. Xu, K. Liu, Z. Hu, K. Deng, S. Zhou, J.-A. Shi, L. Gu, C. Shen, T. Zhang, L. Du, L. Xie, J. Zhu, W. Chen, R. Yang, D. Shi and G. Zhang, *ACS Nano*, 2017, **11**, 12001–12007.

126 D. Dumcenco, D. Ovchinnikov, K. Marinov, P. Lazić, M. Gibertini, N. Marzari, O. L. Sanchez, Y.-C. Kung, D. Krasnozhon, M.-W. Chen, S. Bertolazzi, P. Gillet,

A. Fontcuberta i Morral, A. Radenovic and A. Kis, *ACS Nano*, 2015, **9**, 4611–4620.

127 M. Chubarov, T. H. Choudhury, D. R. Hickey, S. Bachu, T. Zhang, A. Sebastian, A. Bansal, H. Zhu, N. Trainor, S. Das, M. Terrones, N. Alem and J. M. Redwing, *ACS Nano*, 2021, **15**, 2532–2541.

128 D. Reifsnyder Hickey, N. Nayir, M. Chubarov, T. H. Choudhury, S. Bachu, L. Miao, Y. Wang, C. Qian, V. H. Crespi, J. M. Redwing, A. C. T. van Duin and N. Alem, *Nano Lett.*, 2021, **21**, 6487–6495.

129 D. Reifsnyder Hickey, D. E. Yilmaz, M. Chubarov, S. Bachu, T. H. Choudhury, L. Miao, C. Qian, J. M. Redwing, A. C. T. van Duin and N. Alem, *2D Mater.*, 2021, **8**, 011003.

130 X. Xu, Y. Pan, S. Liu, B. Han, P. Gu, S. Li, W. Xu, Y. Peng, Z. Han, J. Chen, P. Gao and Y. Ye, *Science*, 2021, **372**, 195–200.

131 X. Xu, S. Chen, S. Liu, X. Cheng, W. Xu, P. Li, Y. Wan, S. Yang, W. Gong, K. Yuan, P. Gao, Y. Ye and L. Dai, *J. Am. Chem. Soc.*, 2019, **141**, 2128–2134.

132 J. C. Park, S. J. Yun, H. Kim, J.-H. Park, S. H. Chae, S.-J. An, J.-G. Kim, S. M. Kim, K. K. Kim and Y. H. Lee, *ACS Nano*, 2015, **9**, 6548–6554.

133 X. Zhu, A. Li, D. Wu, P. Zhu, H. Xiang, S. Liu, J. Sun, F. Ouyang, Y. Zhou and X. Xiong, *J. Mater. Chem. C*, 2019, **7**, 11650–11650.

134 A. K. Geim and K. S. Novoselov, *Nat. Mater.*, 2007, **6**, 183–191.

135 D. Wickramaratne, L. Weston and C. G. Van de Walle, *J. Phys. Chem. C*, 2018, **122**, 25524–25529.

136 Y. M. Lin, C. Dimitrakopoulos, K. A. Jenkins, D. B. Farmer, H. Y. Chiu, A. Grill and P. Avouris, *Science*, 2010, **327**, 662–662.

137 F. Bonaccorso, Z. Sun, T. Hasan and A. C. Ferrari, *Nat. Photonics*, 2010, **4**, 611–622.

138 S. Roy, X. Zhang, A. B. Puthirath, A. Meiyazhagan, S. Bhattacharyya, M. M. Rahman, G. Babu, S. Susarla, S. K. Saju, M. K. Tran, L. M. Sassi, M. A. S. R. Saadi, J. Lai, O. Sahin, S. M. Sajadi, B. Dharmarajan, D. Salpekar, N. Chakingal, A. Baburaj, X. Shuai, A. Adumbumkulath, K. A. Miller, J. M. Gayle, A. Ajnsztajn, T. Prasankumar, V. V. J. Harikrishnan, V. Ojha, H. Kannan, A. Z. Khater, Z. Zhu, S. A. Iyengar, P. A. d. S. Autreto, E. F. Oliveira, G. Gao, A. G. Birdwell, M. R. Neupane, T. G. Ivanov, J. Taha-Tijerina, R. M. Yadav, S. Arepalli, R. Vajtai and P. M. Ajayan, *Adv. Mater.*, 2021, **33**, 2101589.

139 C. Berger, Z. Song, X. Li, X. Wu, N. Brown, C. Naud, D. Mayou, T. Li, J. Hass, A. N. Marchenkov, E. H. Conrad, P. N. First and W. A. de Heer, *Science*, 2006, **312**, 1191–1196.

140 P. W. Sutter, J.-I. Flege and E. A. Sutter, *Nat. Mater.*, 2008, **7**, 406–411.

141 A. Reina, X. Jia, J. Ho, D. Nezich, H. Son, V. Bulovic, M. S. Dresselhaus and J. Kong, *Nano Lett.*, 2009, **9**, 30–35.